

The Dynamics of Nucleation in Stochastic Cahn–Morrall Systems*

Jonathan P. Desi[†], Hanein H. Edrees[‡], Joseph J. Price[‡], Evelyn Sander[‡], and
Thomas Wanner[‡]

Abstract. Cahn–Morrall systems serve as models for several phase separation phenomena in multicomponent alloys. In this paper we study the dynamical aspects of nucleation in a stochastic version of these models using numerical simulations, concentrating on ternary, i.e., three-component, alloys on two-dimensional square domains. We perform numerical studies and give a statistical classification for the distribution of droplet types as the component structure of the alloy is varied. We relate these statistics to the low-energy equilibria of the deterministic equation.

Key words. Cahn–Morrall systems, nucleation, stochastic partial differential equation, domain exit

AMS subject classifications. 35B40, 35B41, 35K55, 60F10, 60H15, 74N99

DOI. 10.1137/100801378

1. Introduction. Phase separation phenomena in composite materials are of considerable and growing interest. Part of this interest can be attributed to the wealth of intricate phenomena which can be observed. In addition, the implications for the design of new materials plays a significant role. Many composites are formed by combining materials which would not occur naturally within a compound. On the one hand, this is responsible for obtaining materials which exhibit novel and highly desirable properties. On the other hand, this artificial combination of the components can cause problems. In many cases, the composite material is used under service conditions under which its components tend to separate; i.e., the alloy exhibits instability. Since such phase separation can profoundly impact the material properties, understanding this process is extremely important.

In this paper we consider one such phase separation phenomenon of multicomponent metal alloys, known as *nucleation*. If all the components of a metal alloy are heated to a sufficiently high temperature, they will quickly form an almost perfect homogeneous liquid mixture. Upon rapid quenching, the mixture solidifies. After some time, during which the material stays more or less homogeneous, island-like regions form, which are rich in one of the alloy's components. Such regions, called *droplets*, are formed throughout the alloy, destroying

*Received by the editors July 7, 2010; accepted for publication (in revised form) by A. Stuart March 25, 2011; published electronically June 21, 2011.

<http://www.siam.org/journals/siads/10-2/80137.html>

[†]Department of Mathematics and Statistics, University of Maryland, Baltimore County, Baltimore, MD 21250 (jdesi@umbc.edu). This author was supported by an Undergraduate Research Award Scholarship of the University of Maryland, Baltimore County.

[‡]Department of Mathematical Sciences, George Mason University, Fairfax, VA 22030 (hedrees1@gmu.edu, jprice9@gmu.edu, esander@gmu.edu, wanner@math.gmu.edu). The work of the second and third authors was supported by an NSF-CSUMS Grant for Undergraduate Research in Computational Mathematics at George Mason University. The work of the fourth author was partially supported by NSF grants DMS-0639300 and DMS-0907818, and NIH grant R01-MH79502. The work of the fifth author was partially supported by NSF grants DMS-0406231, DMS-0639300, and DMS-0907818, and the U.S. Department of Energy under contract DE-FG02-05ER25712.

the material's homogeneity. They seem to form at random positions, yet they appear to be of a characteristic size. Though the composition of droplets varies, there are only a few types of droplet compositions observed for a given material component structure. In this paper, we study a stochastic partial differential equation model of nucleation in order to explain the classes of droplets which occur for a given alloy composition.

Our multicomponent alloy model is adapted from the celebrated Cahn–Hilliard equation. Specifically, Cahn and Hilliard developed the following partial differential equation to serve as a phenomenological model for phase separation in binary, i.e., two-component, alloys [8, 9, 10], written here in dimensionless form as

$$(1) \quad \begin{aligned} u_t &= -\Delta(\varepsilon^2 \Delta u + f(u)) \quad \text{in } \Omega, \\ \frac{\partial u}{\partial \nu} &= \frac{\partial \Delta u}{\partial \nu} = 0 \quad \text{on } \partial\Omega. \end{aligned}$$

The function u is essentially the difference of the concentrations of the two alloy components as a function of space and time. Thus, u -values close to -1 and 1 correspond to the two pure material components, and values in between correspond to mixtures, with zero representing equal concentrations of both components. The constant $\varepsilon > 0$ is a small dimensionless quantity modeling the interaction length. The domain $\Omega \subset \mathbb{R}^n$ is bounded with appropriately smooth boundary for $n \in \{1, 2, 3\}$, and the function $-f$ is the derivative of a double-well potential F , the standard example being $f(u) = u - u^3$. The Cahn–Hilliard equation generates gradient-like dynamics with respect to the standard van der Waals free energy functional [40]

$$(2) \quad E_\varepsilon[u] = \int_\Omega \left(\frac{\varepsilon^2}{2} \cdot |\nabla u|^2 + F(u) \right) dx.$$

It also conserves the total mass $\int_\Omega u \, dx$. Let μ be defined as the average mass for u ; i.e., let

$$\mu = \frac{1}{|\Omega|} \cdot \int_\Omega u \, dx \quad \text{with} \quad |\Omega| = \int_\Omega 1 \, dx.$$

Using this model, Fife [23] gave the following heuristic explanation for nucleation. After quenching, the alloy is more or less homogeneous, meaning $u \approx \bar{u} \equiv \mu$. The constant function $\bar{u} \equiv \mu$ is an equilibrium solution of (1), and one can easily verify that its stability depends on the sign of the derivative $f'(\mu)$. If μ is contained in the *spinodal region* $\{\mu : f'(\mu) > 0\}$, then the equilibrium \bar{u} is unstable, leading to a sudden phase separation process called *spinodal decomposition*. See, for example, [4, 7, 18, 35, 36, 38, 39, 42]. On the other hand, for μ -values in the *metastable region* $\{\mu : f'(\mu) < 0\}$, the equilibrium \bar{u} is asymptotically stable. While this clearly implies that for small perturbations of \bar{u} the dynamics of (1) drive the system back to the homogeneous state, it is possible that \bar{u} is only a local minimizer of the energy (2). That is, if we perturb the homogeneous equilibrium by a sufficiently large localized disturbance, we might push the system into the domain of attraction of a nonhomogeneous state with lower energy. The solution then approaches the state with lower energy, thereby leading to phase separation.

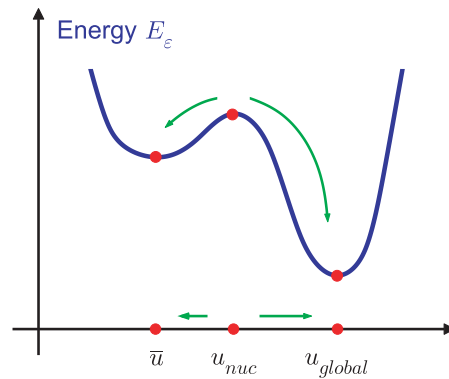


Figure 1. Schematic energy diagram: The homogeneous equilibrium \bar{u} , the canonical nucleus u_{nuc} , and the global minimizer u_{global} .

Bates and Fife [2] confirmed the above intuition for one-dimensional base domains Ω . Namely, they showed that if μ is contained in the metastable region, then the following hold:

- The constant function $\bar{u} \equiv \mu$ is an asymptotically stable equilibrium of the Cahn–Hilliard equation (1).
- There exists an equilibrium solution u_{global} of (1) which is a global minimizer of the energy (2) and which has lower energy than \bar{u} . This solution exhibits exactly one sharp transition layer between the pure states $u = -1$ and $u = +1$.
- In addition, there exists an unstable equilibrium solution u_{nuc} of index 1 such that u_{nuc} is almost everywhere close to μ , except for a small amplitude spike near the boundary of the domain Ω . It is conjectured in [2] that the two branches of the one-dimensional unstable manifold of this solution limit to \bar{u} and u_{global} , respectively.

Thus, if the homogeneous equilibrium \bar{u} is perturbed in the right direction beyond the *critical nucleus* u_{nuc} , then the solution of (1) will follow the unstable manifold of u_{nuc} and converge to the decomposed global energy minimizer u_{global} . See also the diagram in Figure 1. Moreover, the necessary perturbation is relatively small in the sense that it is localized at the boundary of the domain and of a small amplitude. Bates and Fife also describe the actual phase separation dynamics numerically as the solution of (1) follows the unstable manifold. Thus, their results explain the dynamics of nucleation in one space dimension *once the correct type of initial perturbation has been introduced*, and assuming that the unstable manifold of the critical nucleus has the above-stated convergence properties.

The above results do not address the question of how the initial perturbation is generated, or—of crucial importance for materials design—whether the behavior is typical. Further, how long does it typically take before the first droplet nucleates? If this time frame exceeds certain thresholds, we might still be able to characterize the material as stable for all practical purposes. Finally, the observed droplet patterns, rather than attracting, may instead be transient pattern formation and evolve further in important ways.

To address these questions, one has to consider an extension of the Cahn–Hilliard model due to Cook [13], which incorporates random thermal fluctuations into the model. This model is also known as “Model B” in the classification of Hohenberg and Halperin [29]. The *Cahn–*

Hilliard–Cook equation for binary metal alloys is given by

$$(3) \quad \begin{aligned} u_t &= -\Delta(\varepsilon^2 \Delta u + f(u)) + \sigma_{\text{noise}} \cdot \xi \quad \text{in } \Omega, \\ \frac{\partial u}{\partial \nu} &= \frac{\partial \Delta u}{\partial \nu} = 0 \quad \text{on } \partial\Omega, \end{aligned}$$

where the additive noise term ξ is usually chosen as space-time white noise or colored noise. These terms will be explained in more detail later. The parameter σ_{noise} is a measure for the intensity of the noise.

Intuitively, Cahn–Hilliard–Cook models describe the mechanism responsible for the appearance of droplets in nucleation. The random force $\sigma_{\text{noise}} \cdot \xi$ in the right-hand side of (3) will perturb the composition of the alloy away from the homogeneous state \bar{u} , which is thus no longer an equilibrium solution. While in the short term this will not significantly affect the material, the cumulative effect of these perturbations can cause the function u to reach the boundary of the domain of attraction of the homogeneous solution, and to eventually leave the deterministic domain of attraction, moving with probability one towards a state with lower energy. Depending on the strength of the noise—determined by σ_{noise} —this domain exit will take place sooner or later. Different realizations in the noise result in the solution exiting the domain of attraction at a variety of points—leading in turn to different nucleation patterns. However, we show that only a certain small number of resulting droplet classes occur.

In the small-noise limit, domain exit problems such as the one described in the last paragraph can be studied using large deviation-type results; see, for example, [24]. In the context of the one-dimensional Cahn–Hilliard–Cook model, this has recently been accomplished in [3], in which it is shown that for sufficiently small noise intensity, solution paths of the Cahn–Hilliard–Cook model (3) which originate near the homogeneous state $\bar{u} \equiv \mu$ will exit the domain of attraction with probability one, and at the time of exit these paths will be close to the boundary spikes identified in [2]. Understanding part of the attractor structure of (1) lies at the heart of this result. In particular, the results in [3] use the fact that under a basic energy assumption, which has been verified numerically, one branch of the one-dimensional unstable manifold of the spike solution converges to the homogeneous state, while the other branch converges to a phase-separated equilibrium with lower energy than that of $\bar{u} \equiv \mu$. For more details we refer the reader to [26].

In the current paper, we concentrate on a both quantitative and qualitative classification of droplet formation during nucleation on two-dimensional square domains Ω . Rather than considering binary alloys as in [3], we address the more relevant case of multicomponent alloys in the context of a variant of the Cahn–Hilliard–Cook model known as the Cahn–Morral system. This model is described in the next section. We give statistics of large scale simulations showing the types of droplets observed for given overall alloy compositions. We then relate these findings to numerical computations regarding the global attractor structure. Note that *we do not attempt to compute this global attractor structure directly* for the moderately large domains Ω that are used for the evolution simulations. It is numerically infeasible to compute the set all possible (stable and unstable) equilibria in the case of an initial domain that sustains a large number of simultaneous droplets (see, for example, the Cahn–Hilliard study [33], which still considers only fairly small domains). In addition, computing all equilibria would not give insight into the features observed during nucleation: the types of individual droplets

and their geometry. Instead we take an approach which is inspired by recent work of Vanden-Eijnden and Westdickenberg [41], which considers nucleation for the stochastic Allen–Cahn equation, i.e., “Model A” in the classification of Hohenberg and Halperin [29]. In this case, they give analytical results for statistics of droplet formation on a large domain, by decomposing the domain into a large number of smaller fundamental subdomains and then considering nucleation independently on these subsystems. Unfortunately, their results do not carry over to the Cahn–Hilliard or Cahn–Morral situation, due to the global mass conservation in these two systems which results in dependencies between the fundamental domains. Nevertheless, the basic subsystem philosophy of [41] can still be employed, as long as one acknowledges the fact that the effective average masses in the subsystems might deviate from the average mass of the overall large domain. As it turns out, this effective average mass deviation makes it necessary to study the attractor structure of Cahn–Morral systems as a function of the total mass, and we use continuation techniques on small fundamental domains to uncover the structures of interest. We are able to relate the classes of numerically calculated isolated individual equilibrium droplets to the types and frequencies of droplets seen in our statistical simulations.

The remainder of this paper is organized as follows. In section 2 we describe the Cahn–Morral model which forms the basis for our study. This includes both a discussion of the underlying deterministic model and the stability of its homogeneous initial states, as well as a detailed description of the stochastic model extension and the presentation of typical solution paths for the case of ternary alloys. Section 3 contains statistical results for the number and type of droplet solutions as they vary both with time and with the initial composition of the alloy. These are computed by employing computational homological methods that will also be described briefly. Next, in section 4 we present numerical continuation results that shed light on the attractor structure of the deterministic Cahn–Morral system. We begin by establishing numerical continuation results on the droplet equilibria for the deterministic equations on small base domains. For these smaller domains, we use numerical linearization at each of the equilibria and simulation in each of the unstable eigendirections to give a Morse decomposition for the attractor. Subsequently, this information will be used to relate our statistical simulations to the deterministic attractor structure. Finally, section 5 contains conclusions and open questions.

2. Cahn–Morral systems. In this section we present basic definitions and results on the Cahn–Morral model for phase separation in multicomponent alloys. We begin in section 2.1 with a review of the deterministic version of this model. This will be central for our bifurcation analysis in section 4. In section 2.2 we address the question of stability of the homogeneous equilibrium solutions in the deterministic model. Section 2.3 addresses the stochastic extension, which forms the basis for our statistical analysis. In section 2.4 we present some sample solution paths of the stochastic model in order to set the stage for the remainder of this paper.

2.1. The deterministic model. In this section, we describe how the Cahn–Hilliard–Cook system can be extended to a model for the multicomponent case, known as the Cahn–Morral system. We also recall some well-known facts and results about this system. For more details we refer the reader to Morral and Cahn [37], Hoyt [30, 31, 32], Eyre [21, 22], and Maier-Paape, Stoth, and Wanner [34]. We would like to point out that the current paper is

concerned only with the case of ternary, i.e., three-component, alloys. Nevertheless, we will present the stochastic Cahn–Morrall model for the general N -component case, since only the deterministic model had been introduced in the multicomponent situation before [21]. We therefore hope to lay the foundation for the study of more than three components later on using the stochastic extension.

Consider an alloy consisting of $N \geq 3$ components in a bounded domain $\Omega \subset \mathbb{R}^n$, where $n \in \{1, 2, 3\}$. Letting $u_i(t, x) \in [0, 1]$, $i = 1, \dots, N$, denote the concentration of the i th component at time t and location $x \in \Omega$, we have the constraint

$$(4) \quad \sum_{i=1}^N u_i(t, x) = 1 \quad \text{for all } t \geq 0, x \in \Omega;$$

i.e., the values of the vector $u = (u_1, \dots, u_N)$ describing the composition of the alloy are contained in the *Gibbs simplex* \mathcal{G} defined by

$$\mathcal{G} := \left\{ v \in \mathbb{R}^N : \sum_{i=1}^N v_i = 1, v_i \geq 0, i = 1, \dots, N \right\}.$$

With every state $u \in H^1(\Omega, \mathbb{R}^N)$ of the alloy one can associate an energy given by

$$(5) \quad E_\varepsilon[u] = \int_\Omega \left(\frac{\varepsilon^2}{2} \cdot \sum_{i=1}^N |\nabla u_i|^2 + F(u) \right) dx,$$

which is analogous to the van der Waals free energy functional (2) for the case of binary alloys. The parameter $\varepsilon > 0$ models interaction length and is therefore considered to be small. The nonlinear function $F : \mathcal{D} \subset \mathbb{R}^N \rightarrow \mathbb{R}$ represents the bulk free energy density, where the domain \mathcal{D} satisfies $\mathcal{G} \subset \mathcal{D}$, and is defined in more detail below; see, for example, (9) or (10).

As in the binary case, we can use (5) to derive gradient dynamics for the concentration vector $u(t, x)$ which conserves the total mass of each component, i.e., for which

$$(6) \quad \frac{1}{|\Omega|} \cdot \int_\Omega u_i(t, x) dx = \bar{u}_i \quad \text{for all } t \geq 0, i = 1, \dots, N.$$

Define $\mathbf{e} = (1, \dots, 1)^t \in \mathbb{R}^N$, and let $P : \mathbb{R}^N \rightarrow \mathbf{e}^\perp$ denote the orthogonal projection onto \mathbf{e}^\perp , i.e., define $Pu = u - (u, \mathbf{e})/N \cdot \mathbf{e}$. Setting

$$(7) \quad f(u) := -PD_u F(u),$$

we obtain a function from \mathcal{D} into the subspace $\mathbf{e}^\perp \subset \mathbb{R}^N$. The dynamical law associated with (5) is given by the *Cahn–Morrall system*

$$(8) \quad \begin{aligned} u_t &= -\Delta(\varepsilon^2 \Delta u + f(u)) && \text{in } \Omega, \\ \frac{\partial u}{\partial \nu} &= \frac{\partial \Delta u}{\partial \nu} = 0 && \text{on } \partial\Omega, \\ u &\in \mathcal{D} \subset \mathbb{R}^N. \end{aligned}$$

An existence and uniqueness result for solutions of (8) in the special case of \mathcal{D} being the simplicial interior of the Gibbs simplex \mathcal{G} can be found in Elliott and Luckhaus [20] for the logarithmic potential

$$(9) \quad F(u_1, \dots, u_N) = \sigma \cdot \sum_{1 \leq i < j \leq N} u_i u_j + \sum_{i=1}^N u_i \ln u_i.$$

However, as described in more detail in the next section, this nonlinearity is not appropriate in our case since we are adding noise to the Cahn–Morrall model. For the purposes of this paper, instead of considering the potential F defined in (9), we consider a potential which is defined on all of $\mathcal{D} = \mathbb{R}^N$ but has qualitative features similar to those of the logarithmic potential. More precisely, we use the polynomial nonlinearity

$$(10) \quad F(u_1, \dots, u_N) = \prod_{i=1}^N \left(u_1^2 + \dots + u_{i-1}^2 + \sigma \cdot (u_i - 1)^2 + u_{i+1}^2 + \dots + u_N^2 \right),$$

where $\sigma > 0$ is some parameter. This potential is symmetric in its variables and has global minima exactly at the vertices of the Gibbs simplex \mathcal{G} , corresponding to the pure materials. For the nonlinearity in (10), the states $u(t, x)$ are no longer restricted to the Gibbs simplex \mathcal{G} —even though they will stay close to it. This situation is completely analogous to the classical binary Cahn–Hilliard model, where the order parameter is not restricted to the interval $[-1, 1]$.

2.2. Deterministic stability of the homogeneous state. As in the case of the Cahn–Hilliard model discussed in the introduction, spatially constant functions are equilibrium solutions for the Cahn–Morrall system (8). In the context of nucleation, one has to consider solutions of the Cahn–Morrall system which originate near such a homogeneous state in the Gibbs simplex \mathcal{G} . Nucleation is possible only if this state is asymptotically stable for the deterministic system. In the current section, we identify those homogeneous states.

To this end, fix a homogeneous state $\bar{u} = (\bar{u}_1, \dots, \bar{u}_N)$ satisfying (4). Define B as the Jacobian of f at \bar{u} ; i.e., let $B = -PD_u^2 F(\bar{u})$. Then the linearization of (8) at the homogeneous state \bar{u} is given by

$$(11) \quad \begin{aligned} v_t &= -\Delta(\varepsilon^2 \Delta v + Bv) && \text{in } \Omega, \\ \frac{\partial v}{\partial \nu} &= \frac{\partial \Delta v}{\partial \nu} = 0 && \text{on } \partial\Omega, \\ v_1 + \dots + v_N &= 0. \end{aligned}$$

Notice that the matrix B is not symmetric in general. However, since B corresponds to a linear map from \mathbb{R}^N into the $(N - 1)$ -dimensional subspace \mathbf{e}^\perp , it always has an eigenvalue of zero. Furthermore, one can easily show that the restriction of this linear map to the invariant subspace \mathbf{e}^\perp is in fact symmetric. In the following we denote the \mathbb{R}^N -orthonormal eigenvectors of B restricted to the subspace \mathbf{e}^\perp by w_1, \dots, w_{N-1} , with corresponding real eigenvalues $\beta_1 \geq \beta_2 \geq \dots \geq \beta_{N-1}$. For our discussion of the stability of the homogeneous states, we also need the following definition.

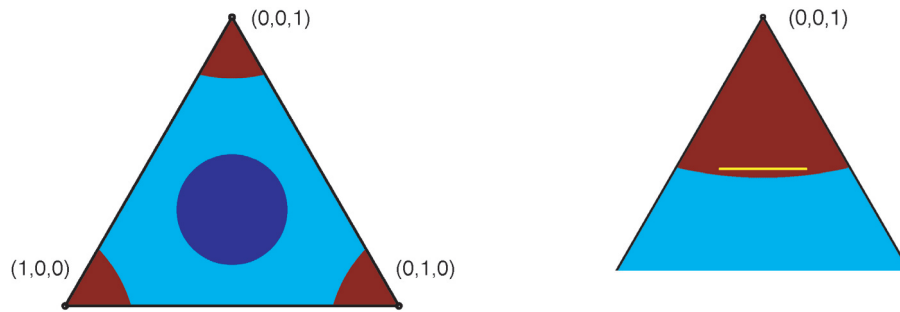


Figure 2. Stability diagram for the homogeneous equilibrium \bar{u} of a three-component alloy for the nonlinearity (10) with value $\sigma = 3.5$, which will be kept fixed throughout the numerical parts of the paper. The stability of \bar{u} depends on the location of \bar{u} in the Gibbs simplex, whose projection is shown in the left image. The red region corresponds to the metastable region, light blue to the portion of the spinodal region with one positive eigenvalue of B , and dark blue to the portion with two positive eigenvalues. The right image shows a blow-up of one of the corner regions. In some of our simulations, we restrict our analysis to the set of homogeneous equilibrium states on the portion of the yellow line segment $\bar{u} = (\alpha + \beta, \alpha - \beta, 1 - 2\alpha)$ inside the metastable region, which is shown for $\alpha = 0.10$ and $|\beta| \leq 0.05$.

Definition 2.1. Let $\Omega \subset \mathbb{R}^n$, with $n \in \{1, 2, 3\}$, denote a bounded domain with sufficiently smooth boundary, and consider the negative Laplacian $-\Delta : L^2(\Omega) \rightarrow L^2(\Omega)$ subject to homogeneous Neumann boundary conditions. Then its eigenvalues are denoted by $0 = \kappa_0 < \kappa_1 \leq \kappa_2 \leq \dots \rightarrow +\infty$, and the corresponding $L^2(\Omega)$ -orthonormalized eigenfunctions are given by $\varphi_0, \varphi_1, \varphi_2, \dots$.

In order to determine the stability of the equilibrium \bar{u} we look for solutions of (11) of the form $v(t, x) = e^{\lambda t} \cdot w \cdot \psi(x)$, where $w \in \mathbf{e}^\perp \subset \mathbb{R}^N$ is an eigenvector of the matrix B and ψ is an eigenfunction of the negative Laplacian. Using the notation introduced above, one can easily show that the spectrum of the linearized equation (11) is given by the eigenvalues

$$\lambda_{i,k,\varepsilon} = \kappa_i \cdot (\beta_k - \varepsilon^2 \cdot \kappa_i) \quad \text{for } i \in \mathbb{N}, 1 \leq k \leq N - 1,$$

with corresponding eigenfunctions $w_k \cdot \varphi_i(x)$. The homogeneous state \bar{u} is asymptotically stable for (8), provided that all of these eigenvalues are negative. Thus we have proved the following result.

Lemma 2.2. The homogeneous equilibrium \bar{u} is asymptotically stable for every $\varepsilon > 0$ for the deterministic Cahn–Morrall system (8) if the largest eigenvalue of the matrix $B = -PD_u^2 F(\bar{u})$ restricted to the subspace \mathbf{e}^\perp is strictly negative, i.e., provided that one has $\beta_1 < 0$.

Homogeneous states with $\beta_1 < 0$ are therefore the ones which could trigger nucleation in the stochastic Cahn–Morrall system defined below in (12). We call the collection of all these states the *metastable region* of the hyperplane $u_1 + \dots + u_N = 1$, and its complement the *spinodal region*. In Figure 2 these regions are shown for the ternary special case $N = 3$, and for the parameter value $\sigma = 3.5$ in (10). The metastable region is shown in red and is located around the pure materials, which correspond to the three corners of the Gibbs triangle. The spinodal region is further divided into a light blue part and a dark blue part, corresponding to $\beta_1 > 0 > \beta_2$ and $\beta_1 \geq \beta_2 > 0$, respectively.

2.3. The stochastic model. Ideally, one would like to pass to a stochastic version of the above model by adding additive noise as in the Cahn–Hilliard–Cook equation (3), and this in turn restricts the choice of nonlinearity. Namely, any form of additive noise will drive solution paths of the resulting stochastic evolution equation outside the Gibbs simplex with probability one, and the logarithmic potential (9) is undefined there. While this could be avoided by introducing suitable multiplicative noise, we employ a different strategy. In contrast to the Cahn–Morral system with the logarithmic nonlinearity, the values of u in the standard Cahn–Hilliard equation are not restricted to a finite interval. Following Grant [27], we therefore drop the nonnegativity condition on the components u_i and retain only constraint (4). This explains our use of the nonlinearity defined by (10) instead of (9), since the potential F in (10) is well defined outside the nonnegative region of the Gibbs simplex. Like the model of Grant—or even the deterministic Cahn–Hilliard equation—our choice of nonlinearity guarantees only that with high probability solutions stay close to the Gibbs simplex for which there is nonnegative mass. Our choice of nonlinearity always preserves total mass, i.e., $u_1 + \cdots + u_N = 1$. Specifically, the system used in this paper is formed using the nonlinearity f from (7), using (10) with an added noise term, giving the *stochastic Cahn–Morral system* in the form

$$(12) \quad \begin{aligned} u_t &= -\Delta(\varepsilon^2 \Delta u + f(u)) + \sigma_{\text{noise}} \cdot \xi && \text{in } \Omega, \\ \frac{\partial u}{\partial \nu} &= \frac{\partial \Delta u}{\partial \nu} = 0 && \text{on } \partial\Omega, \\ u_1 + u_2 + \cdots + u_N &= 1. \end{aligned}$$

Adding the noise term ξ has to be done carefully—as will be described in more detail in the remainder of this section. We begin by recalling the precise form of the stochastic perturbation in the Cahn–Hilliard–Cook model (3). For this, recall Definition 2.1 from the previous section. Then the noise process ξ in (3) is defined on an abstract probability space $(\mathbb{F}, \mathcal{F}, \mathbb{P})$, and it is given as the generalized derivative of some Q -Wiener process $\mathcal{W}(t)$, for $t \geq 0$, defined explicitly as a generalized Fourier expansion of the form

$$(13) \quad \mathcal{W}(t) = \sum_{k=1}^{\infty} \alpha_k \cdot \beta_k(t) \cdot \varphi_k \quad \text{with } Q\varphi_k = \alpha_k^2 \varphi_k.$$

In this series, the sequence $(\beta_k)_{k \in \mathbb{N}}$ consists of independent real-valued standard Brownian motions over $(\mathbb{F}, \mathcal{F}, \mathbb{P})$, and the operator Q denotes the covariance operator of \mathcal{W} . Notice in particular that the series does not include the constant eigenfunction φ_0 from Definition 2.1, which ensures that all solution paths of the stochastic partial differential equation (3) preserve the total mass. In other words, the identity (6) is satisfied along any solution path of (3). For more details we refer the reader to Blömker, Maier-Paape, and Wanner [4], Da Prato and Debussche [14], as well as to the monograph by Da Prato and Zabczyk [15].

While it would be tempting to define the noise process in (12) as $\xi = (\xi_1, \dots, \xi_N)$, with independent component processes ξ_i as in (13), such a definition would cause the constraint $u_1 + \cdots + u_N = 1$ to be violated for almost all solution paths. Thus, we use the following definition.

Definition 2.3. Let ξ_1^*, \dots, ξ_N^* denote independent noise processes defined over a common probability space $(\mathbb{F}, \mathcal{F}, \mathbb{P})$ such that each ξ_ℓ^* is the generalized derivative of a Q -Wiener process $\mathcal{W}_\ell(t)$, $t \geq 0$, defined by

$$(14) \quad \mathcal{W}_\ell(t) = \sum_{k=1}^{\infty} \alpha_k \cdot \beta_{\ell,k}(t) \cdot \varphi_k \quad \text{with } Q\varphi_k = \alpha_k^2 \varphi_k.$$

As before, the sequences $(\beta_{\ell,k})_{k \in \mathbb{N}}$ denote independent real-valued Brownian motions over $(\mathbb{F}, \mathcal{F}, \mathbb{P})$, and the φ_k are introduced in Definition 2.1. Then we define the noise process $\xi = (\xi_1, \dots, \xi_N)$ in (12) as

$$(15) \quad \xi = P\xi^* \quad \text{with } \xi^* = (\xi_1^*, \dots, \xi_N^*),$$

where $P: \mathbb{R}^N \rightarrow \mathbf{e}^\perp$ denotes the orthogonal projection onto the orthogonal complement of the vector $\mathbf{e} = (1, \dots, 1)^t \in \mathbb{R}^N$.

With this definition, the constraint $u_1 + \dots + u_N = 1$ is satisfied along every solution path. Furthermore, the noise process ξ is isotropic in the sense that the projection of $\xi(t)$ onto any unit vector in \mathbf{e}^\perp has the same distribution, and that projections onto orthogonal vectors furnish independent random variables.

The real sequence $(\alpha_k)_{k \in \mathbb{N}}$ in Definition 2.3 affects the spatial smoothness of the noise process ξ , and therefore also the regularity of the solutions of (12). In particular, we are interested in solutions which are contained in the Sobolev space

$$H^2(\Omega)^N = \underbrace{H^2(\Omega) \times \dots \times H^2(\Omega)}_{N \text{ factors}}$$

and satisfy homogeneous Neumann boundary conditions. Notice that this is exactly the functional-analytic setup that is usually used for describing the dynamics of Cahn–Hilliard-type evolution equations, and this ensures via Sobolev’s embedding theorem [1] that the solutions are continuous with respect to the spatial variables. The following result can be obtained using standard arguments.

Theorem 2.4. Consider the stochastic Cahn–Morral system (12) for the potential F defined in (10), and let the noise process ξ be defined as in Definition 2.3. Furthermore, assume that the real sequence $(\alpha_k)_{k \in \mathbb{N}}$ satisfies the condition

$$(16) \quad \limsup_{k \rightarrow \infty} (\alpha_k^2 \cdot \kappa_k^{s_{\mathcal{R}}}) < \infty, \quad \text{where } s_{\mathcal{R}} > \frac{\dim \Omega}{2}.$$

Then for every initial condition $u_0 \in H^2(\Omega)^N$ the stochastic Cahn–Morral system (12) has a unique local mild solution u such that $u(t) \in H^2(\Omega)^N \subset C(\bar{\Omega})^N$ for almost all solution paths.

Proof. According to [4, 5, 15] the existence of a unique local mild solution in the Sobolev space $H^2(\Omega)^N$ can be established as long as $s_{\mathcal{R}} > \dim \Omega / 2$. More precisely, one can directly apply [5, Theorem 3.1]; see also [6, Proposition 2.10]. ■

The above result will suffice for the purposes of this paper. We would like to point out, however, that it is possible to relax the conditions on the regularity of the noise process

significantly if one drops the requirement of finding mild solutions in $H^2(\Omega)^N$. For example, in [3] it is shown for the one-dimensional case that existence in the space of continuous functions can be established even with $s_{\mathcal{R}} = -1$; i.e., even if the noise process ξ is the spatial derivative of space-time white noise. Related results can be found in [11].

For the simulations of the stochastic system (12) in the present paper we generally consider the case of cut-off noise, which is widely used in the physics literature. In other words, we consider $\alpha_k = 1$ for $k = 1, \dots, M$, and $\alpha_k = 0$ otherwise. The constant M is chosen large enough to make sure that all eigenfunctions of the linearized Cahn–Morrall system (11) with wave numbers larger than M are strongly stable; i.e., their eigenvalues are significantly negative.

2.4. Sample evolution paths. In order to illustrate some aspects of the nucleation dynamics of Cahn–Morrall systems, we present sample solution paths for (12). We exclusively address the case of ternary alloys, i.e., $N = 3$, while focusing on the metastable region—the red region in Figure 2—where nucleation occurs. From now on, we denote the function (u_1, u_2, u_3) by (u, v, w) and use the value $\sigma = 3.5$ in (10).

For the classical Cahn–Hilliard equation (1) for binary alloys, there are two central parameters: the interaction length ε and the average mass μ of the order parameter u . The Cahn–Morrall system for ternary alloys involves three parameters: one to specify the interaction length ε as before and two parameters to specify the unique homogeneous state associated with the average masses of the three components. For convenience, we will change notation to the parameters λ , α , and β , as defined below. To begin with, rather than considering small ε values approaching zero, we use the parameter λ defined as

$$(17) \quad \lambda = \frac{1}{\varepsilon^2}.$$

The introduction of λ follows the convention generally seen in bifurcation analyses. Rather than studying the limit $\varepsilon \rightarrow 0$, our bifurcation analysis of section 4 will consider the case of large λ . Furthermore, rather than specifying the average masses of two of the components, we choose to take advantage of the symmetry of the equation in our choice of parameters. Thus our two parameters α and β are chosen such that α measures the average mass of the arithmetic mean $(u + v)/2$ of the components u and v , and β measures the average mass of $(u - v)/2$. That is,

$$(18) \quad (\bar{u}, \bar{v}, \bar{w}) = (\alpha + \beta, \alpha - \beta, 1 - 2\alpha).$$

This choice has the advantage that we recover the complete information about solution behavior by considering only the parameter range

$$\mathfrak{R} = \{(\alpha, \beta) : 0 \leq \alpha \leq 1/3, |\beta| \leq \alpha\},$$

which corresponds to the top part of the Gibbs triangle shown in Figure 2. One has only to note that if (u, v, w) is a solution of (12) with average mass $(\bar{u}, \bar{v}, \bar{w})$, then (v, u, w) is a solution with average mass $(\bar{v}, \bar{u}, \bar{w})$, and similarly for any other permutation of the three components. If we keep α fixed, then the points $(\bar{u}, \bar{v}, \bar{w})$ in (18) with $|\beta| \leq \alpha$ form a line which is parallel to the base of the Gibbs triangle. For most of our simulations of (12) we consider the case $\alpha = 0.1$

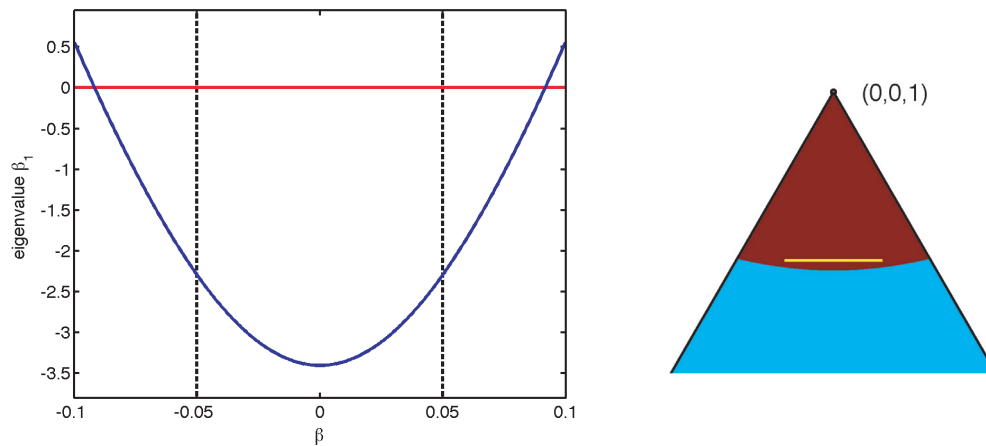


Figure 3. The left graph shows the dependence of the eigenvalue β_1 from Lemma 2.2 on the parameter β for fixed $\alpha = 0.1$. The corresponding homogeneous states $(\bar{u}, \bar{v}, \bar{w})$ for $|\beta| \leq 0.05$ lie on the yellow line in the right-hand image.

and $|\beta| \leq 0.05$, which corresponds to the yellow line in the right-hand image of Figure 2. This yellow line is shown again in the right-hand image of Figure 3, which contains a blow-up of the top part of the Gibbs triangle. The graph on the left shows the values of the eigenvalue β_1 introduced before Lemma 2.2. This graph shows that for $\alpha = 0.1$ and $|\beta| \leq 0.05$ the initial conditions $(\bar{u}, \bar{v}, \bar{w})$ are contained in the metastable region. Notice, however, that for $\alpha = 0.1$ and β values close to -0.1 or 0.1 one enters the spinodal region.

Figure 4 shows six solution snapshots of a sample solution path of (12) for the two-dimensional domain $\Omega = (0,1)^2$, where $\lambda = 400$ (i.e., we have $\varepsilon = 0.05$) and the noise strength is given by $\sigma_{\text{noise}} = 0.2$. The simulation has as its initial state the homogeneous state $(\bar{u}, \bar{v}, \bar{w}) = (0.1, 0.1, 0.8)$, which lies in the metastable region, more precisely, at the center of the yellow line in Figure 3. For this initial state, the nonzero eigenvalues of B are given by $\beta_1 \approx -3.4$ and $\beta_2 \approx -22.5$ in Lemma 2.2. In order to illustrate the alloy composition as a function of space, we make use of the fact that the potential (10) used in our simulations has global minima at the corners of the Gibbs simplex. This implies that for a phase separated alloy at fixed time t , the range of the vector-valued function $x \mapsto (u(t, x), v(t, x), w(t, x))$ will be concentrated in a small neighborhood of the Gibbs simplex, and we can use this three-dimensional vector as an RGB value (after projecting points outside the Gibbs simplex to the closest point on the Gibbs simplex). In this way, one obtains an image which represents the alloy composition as a function of space, with the colors red, green, and blue corresponding to the pure u , v , and w components, respectively. Mixtures of these main components are indicated through mixtures of the pure colors.

The six RGB plots in Figure 4 correspond to six values of the time t of a solution path originating at the homogeneous state $(\bar{u}, \bar{v}, \bar{w}) = (0.1, 0.1, 0.8)$; i.e., we consider the case $\alpha = 0.1$ and $\beta = 0$. While no nucleation has taken place in the first snapshot, in the second snapshot one can see the appearance of small droplets. We would like to point out that while some of these initial droplets are pure, i.e., red or green, some of the initial droplets appear to consist of an equal homogeneous mixture of both of these components. By the third snapshot,

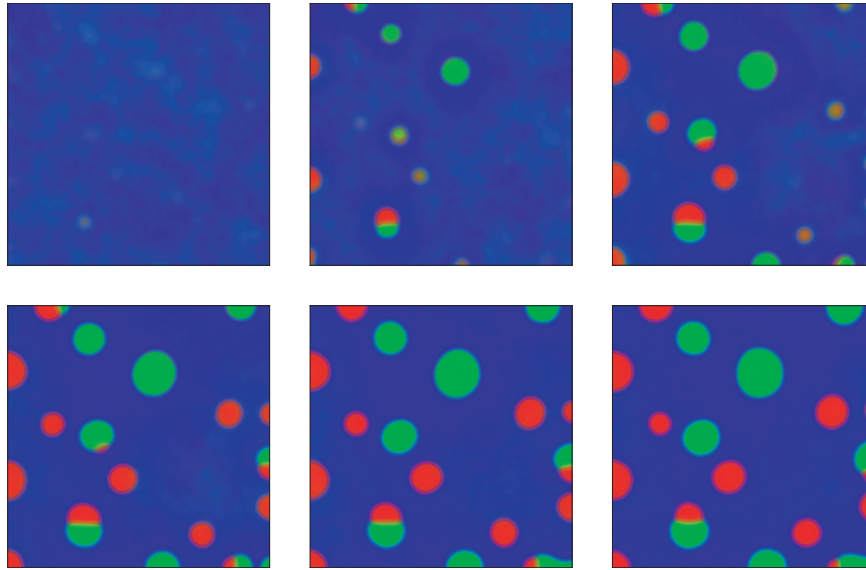


Figure 4. Sample evolution in two space dimensions, starting at the homogeneous equilibrium $(\bar{u}, \bar{v}, \bar{w}) = (0.1, 0.1, 0.8)$, for $\lambda = 400$ (i.e., $\varepsilon = 0.05$) and $\sigma_{\text{noise}} = 0.2$. Starting from the top left, the figures correspond to times $t = k \cdot 2.1 \cdot 10^{-4}$ for $k = 1, \dots, 6$.

the initial droplets have grown, and more droplets have nucleated. The compositions of these later stage single droplets are either close to $(1, 0, 0)$ (red), which we call a *u-droplet*, or close to $(0, 1, 0)$ (green), which we call a *v-droplet*. Notice also that some droplets form with both *u*- and *v*-components separated by an internal interface. We refer to this as a *double droplet*. In the last three snapshots, there is little change in the number and type of droplets that have formed. Notice also that while the *u*-droplets and *v*-droplets appear with similar frequency, double droplets are significantly less likely to occur.

In order to get an impression of the final droplet geometries and compositions that can be observed for different β -values, Figure 5 shows RGB plots of snapshots at one fixed time for $\alpha = 0.1$ and a variety of values of β . While individual droplet types are similar to those observed for $\beta = 0$, the frequency with which these types occur does seem to depend on β . The snapshots indicate that as β grows more positive, the first component starts to dominate. Thus, we see progressively fewer *v*-droplets and fewer double droplets for increasing β . Notice in particular that the last two snapshots do not contain any double droplets. All of these observations will be quantified statistically in section 3.

The above simulations show only a few specific solution paths of the stochastic Cahn–Morrall system (12). Nevertheless, they showcase certain features of the nucleation process which will be explained in more detail in the remainder of the paper. In fact, these features are not restricted to the case of two-dimensional domains. We have observed analogous behavior also in one and three space dimensions. For the remainder of the present paper, however, we concentrate on only the two-dimensional situation.

3. A statistical analysis of nucleation simulations. In this section, we present statistical information obtained from Monte Carlo simulations of solutions to the stochastic Cahn–Morrall

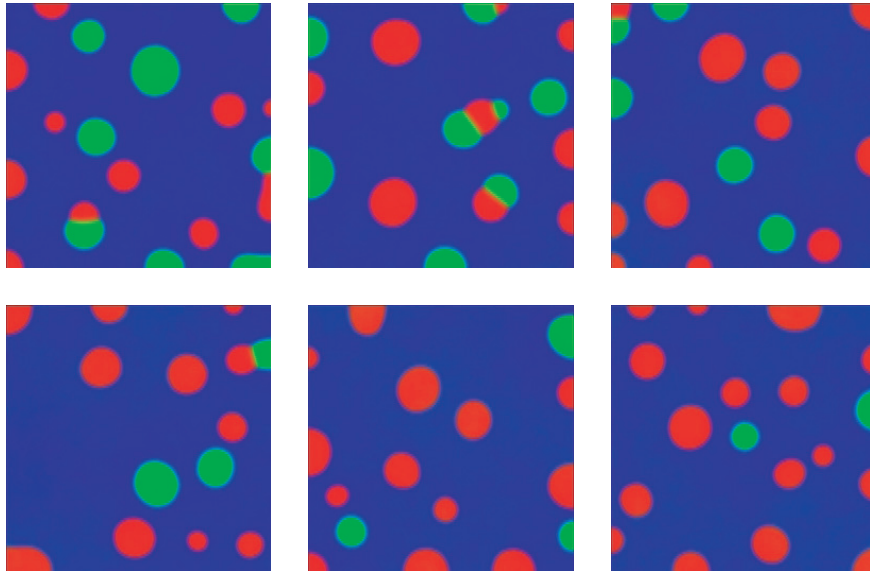


Figure 5. Solution snapshots in two space dimensions for $\alpha = 0.1$ and six β -values. Starting from the top left, the figures correspond to β -values $k \cdot 0.005$ for $k = 0, \dots, 5$. Each of the simulations start at the homogeneous state $(\bar{u}, \bar{v}, \bar{w}) = (0.1 + \beta, 0.1 - \beta, 0.8)$ for $\lambda = 400$ and $\sigma_{\text{noise}} = 0.2$. All of the snapshots are at the fixed time $t = 15 \cdot 10^{-4}$.

equation (12) in two space dimensions for a variety of parameter values. As indicated in the sample runs of the previous section, there are three predominant types of nucleating solutions observed in simulations in the nucleation region: u -droplets, v -droplets, and double droplets. For a variety of different initial mass vectors $(\bar{u}, \bar{v}, \bar{w})$ we compute quantitative information on the total number and the proportion of each type of droplet as a function of time. In addition, we distinguish droplet formation in the domain interior, along the edges of the domain, and at the four corners. In section 3.1 we describe the various numerical methods that were employed for our study, and section 3.2 contains droplet statistics both as a function of time and as a function of the initial mass vector. Finally, section 3.3 addresses the question of the suitability of the interaction parameters used for our simulations with the help of domain scaling techniques.

3.1. Numerical methodology. We begin by briefly describing the numerical methods that were used to obtain our results on the nucleation statistics. All simulations of the stochastic Cahn–Morral model (12) were performed using a semi-implicit spectral Galerkin method which—due to the assumed Neumann boundary conditions—approximates the solution $u(t)$ via a truncated cosine series. The specific implementation used for this study is similar to the one that has been discussed in [28] in the context of stochastic phase-field models. We refer the interested reader to that paper for a more detailed study, including error estimates.

In order to obtain the droplet statistics presented in section 3.2 below, we performed Monte Carlo-type simulations originating at random perturbations of certain homogeneous initial states $(\bar{u}, \bar{v}, \bar{w})$. For all simulations, we consider the domain $\Omega = (0, 1)^2$ with $\varepsilon = 0.05$; i.e., we assume $\lambda = 400$. The noise intensity is chosen as $\sigma_{\text{noise}} = 0.2$. At every time step, the solution $u(t, \cdot)$ is approximated by 128^2 spectral modes, and we use a step size of

$\Delta t = 10^{-8}$ along the solution paths. All of the simulations have initial time $t = 0$ and end at $t_{\text{end}} = 0.0015$. The simulations originate at small random perturbations of the homogeneous initial states $(\bar{u}, \bar{v}, \bar{w}) = (\alpha + \beta, \alpha - \beta, 1 - 2\alpha)$, where we fix $\alpha = 1/10$ and consider $\beta = k/400$ for $k = 0, \dots, 20$. For each of the 20 initial states with $k > 0$ we performed a set of 512 simulations, and in the symmetric case $k = 0$ we computed 1024 solution paths.

The parameter settings described in the previous paragraph were used for all the simulation results which will be presented in section 3.2. In addition, we validated our findings with a second set of simulations for smaller interaction length, but on the same domain $\Omega = (0, 1)^2$. For this, we consider $\varepsilon = 0.02$; i.e., we choose $\lambda = 2500$. The noise intensity is left unchanged at $\sigma_{\text{noise}} = 0.2$, but at every time step the solution $u(t, \cdot)$ is now approximated by 256^2 spectral modes. Finally, we use a step size of $\Delta t = 2 \cdot 10^{-9}$ between $t = 0$ and $t = 0.0002$. The simulations originate at small random perturbations of the homogeneous initial states $(\bar{u}, \bar{v}, \bar{w}) = (\alpha + \beta, \alpha - \beta, 1 - 2\alpha)$, where we again fix $\alpha = 1/10$, but now consider $\beta = k/200$ for $k = 0, \dots, 10$. For each of the 10 initial states with $k > 0$ we performed a set of 128 simulations; for $k = 0$ we again computed 1024 solution paths. While the results of these validation simulations will not be presented in detail, they were used in part to validate our main set of simulations. Finally, in order to further understand the dependence of our results on the interaction length ε , we also performed simulations for $\varepsilon = 0.04, 0.03, 0.01$, and 0.005 . In each of these cases, we considered only $\alpha = 1/10$ and $\beta = 0$ and determined the solution paths into the beginning of the coarsening regime. The results from these simulations will be discussed in section 3.3.

In addition to the actual numerical solution of the stochastic evolution equation (12), we use methods from computational topology to automatically determine the number of droplets of each type. For this, we employ standard thresholding techniques to obtain subsets X of Ω which show the location of u -droplets, v -droplets, and double droplets. In order to minimize numerical artifacts, these sets are smoothed using a convolution filter, before the Betti numbers $\beta_0(X)$ and $\beta_1(X)$ of the sets X so obtained are determined using the program package CHomP [12]. Recall that the zero-dimensional Betti number $\beta_0(X)$ counts the number of connected components of the set X , while the first Betti number $\beta_1(X)$ equals the number of holes in X . Similar to the approach in [25], we use basic results from planar topology to distinguish between droplets in the interior of the domain and droplets which touch the boundary. As is described in more detail in [25], it is possible to achieve this distinction by determining the Betti numbers not only of a given thresholded set X , but also of its complement $\Omega \setminus X$. Since an interior component of X gives rise to a hole in $\Omega \setminus X$, the set X has $\beta_1(\Omega \setminus X)$ interior components as well as $\beta_0(X) - \beta_1(\Omega \setminus X)$ components which touch the boundary.

Finally, due to the stochastic nature of our simulations, we include confidence intervals with the computed mean values for the considered quantities. For this we use studentized bootstrap confidence intervals for the given stochastic data. The cutoff levels for the percentiles are p and $1 - p$; i.e., we compute $1 - 2p$ confidence intervals. Throughout this paper we use $p = 0.025$, which results in 95% confidence intervals. The bootstrap computations use 1000 bootstrapped sample data sets, as described in [16, section 5.2.1, p. 194].

3.2. Droplet statistics from Monte Carlo simulations. In this section we present statistical information on droplet formation during nucleation in the stochastic Cahn–Morrall

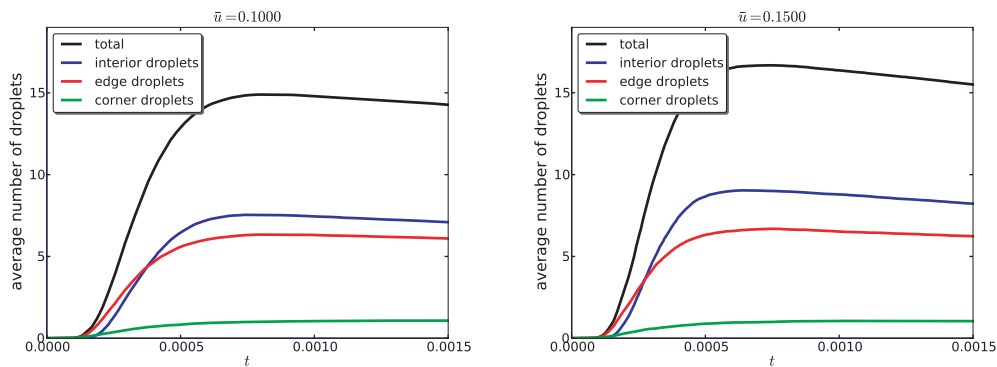


Figure 6. Averaged number of droplets as a function of time, organized by nucleation location. The graphs show the averaged total number of droplets (black), as well as the average number of interior droplets (blue), droplets which touch one of the edges of Ω (red), and droplets which touch the corners of the domain (green). The left image is for $\alpha = 1/10$ and $\beta = 0$ in (18), the right image for $\alpha = 1/10$ and $\beta = 1/20$. The images show that the change in mass does not significantly change the qualitative form of the evolution curves. Furthermore, droplets tend to nucleate first at the boundary, and only at later times in the interior of the domain.

system (12). As mentioned in section 3.1, these results are obtained from Monte Carlo simulations for $\lambda = 1/\varepsilon^2 = 400$, for initial mass vectors $(\bar{u}, \bar{v}, \bar{w})$ as in (18) with $\alpha = 1/10$ and varying β . This particular parameter combination was chosen to obtain reasonable simulation times based on a relatively small number of unstable modes, and we will briefly discuss the validation of our observations on several occasions below.

We begin by considering the temporal evolution of the various droplet counts. The two graphs in Figure 6 are concerned with the likelihood of droplet locations as a function of time. We distinguish between droplets which are located at one of the corners of the base domain $\Omega = (0, 1)^2$, along the boundary edges of this domain, or in the interior of the domain. The curves in Figure 6 depict averaged droplet counts over all the Monte Carlo simulations. Before discussing the behavior of the droplet counts as a function of time, we would like to point out that the qualitative form of the evolution curves seems to be almost unchanged for the two mass concentrations shown in Figure 6—which are given by $\bar{u} = 0.1$ and $\bar{u} = 0.15$ for the left and right images, respectively. In fact, this lack of variability can be observed throughout the β -values that were considered for our simulations. Turning our attention to the actual time dependence, the graphs in Figure 6 indicate that droplets tend to nucleate first along the boundary of the domain and only later in the interior. Furthermore, the various droplet counts reach their maximum levels at about the same time, before then settling into a slow coarsening process. When the maximum droplet counts are achieved, there are more droplets in the interior of the domain than along the boundary, even though for the chosen ε the average droplet counts are very close to each other and fairly small. While at first glance this closeness of the droplet counts might indicate that the domain size for our simulations is too small, in fact the opposite is true. This will be discussed extensively in section 3.3 below.

To close this section, we turn our attention to the variation of the various droplet measures as a function of the concentration $(\bar{u}, \bar{v}, \bar{w})$ of the initial homogeneous state. As before, we consider concentration vectors as defined in (18) with fixed $\alpha = 1/10$ and varying β . Moreover, we consider our Monte Carlo simulations for $\varepsilon = 0.05$, but this time at the fixed time

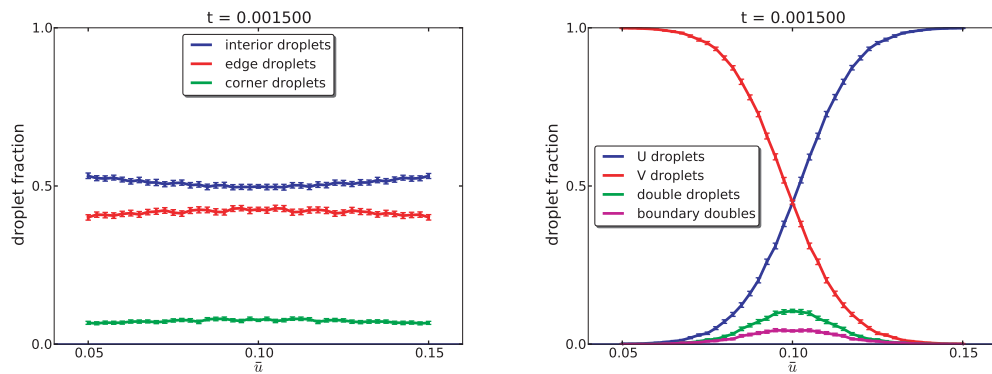


Figure 7. Averaged number of droplets as a function of \bar{u} , organized by nucleation location (left panel) and by droplet composition (right panel). Both graphs consider solution information at time $t = 0.0015$ and show the fractions observed for each droplet location or type, including bootstrap confidence intervals. The left image shows the droplet fractions for droplets in the interior (blue), along the edges (red), and in the corners (green) of the domain Ω . The right image depicts the fractions of u -droplets (blue), v -droplets (red), double droplets (green), and double droplets which touch the boundary (purple).

$t = 0.0015$. The resulting graphs are depicted in Figure 7, which also includes bootstrap confidence intervals for the data points as described in the previous section. In order to visualize the dependence of the droplet fractions over the interval $0.05 \leq \bar{u} \leq 0.15$ we use symmetry properties of our Cahn–Morrall system (12). One can easily show that for any solution path $(u(t), v(t), w(t))$ with concentration vector $(\bar{u}, \bar{v}, \bar{w})$, the permutation $(v(t), u(t), w(t))$ is a solution path of (12) with concentration vector $(\bar{v}, \bar{u}, \bar{w})$. In other words, the droplet fractions for any concentration $\bar{u} = \mu < 0.1$ can be determined from the droplet fractions for the concentration $\bar{u} = 0.2 - \mu > 0.1$, by simply changing the role of u and v .

The left-hand panel of Figure 7 contains the information pertaining to the droplet location. As we already mentioned earlier, the temporal evolution for various values of the concentration vectors seemed to indicate that the preferred droplet locations hardly change with the concentration. The graphs in the left panel of Figure 7 seem to confirm this. For all considered \bar{u} -values, the fraction of interior or boundary droplets remains fairly constant. While for the specific ε -value considered in these simulations both fractions are close to 50%, the ratios diverge as ε decreases towards zero. This is confirmed by our simulations for smaller ε -values. Nevertheless, the almost constant dependence on \bar{u} persists.

Significantly more interesting is the right-hand panel of Figure 7, which contains the variation of droplet type as a function of \bar{u} . The fraction of u -, v -, and double droplets clearly depends on \bar{u} , with more u -droplets for larger \bar{u} , more v -droplets for smaller \bar{u} , and about even numbers of u - and v -droplets when $\bar{u} = \bar{v}$. The curve for the fraction of u -droplets has a rather sharp increase, and for $\bar{u} > 0.13$ almost all droplets are u -droplets. Similarly, for $\bar{u} < 0.07$ almost all droplets are v -droplets. Both in the interior of the region and on the boundary, the number of double droplets is largest for the symmetric case $\bar{u} = 0.1$. Furthermore, outside the region $0.06 < \bar{u} < 0.14$, there appear to be no double droplets occurring. We are able to explain this in the next section. Specifically, we demonstrate that the energy of the double droplet solutions is smaller than the energy of single droplet solutions on an interval of \bar{u} -

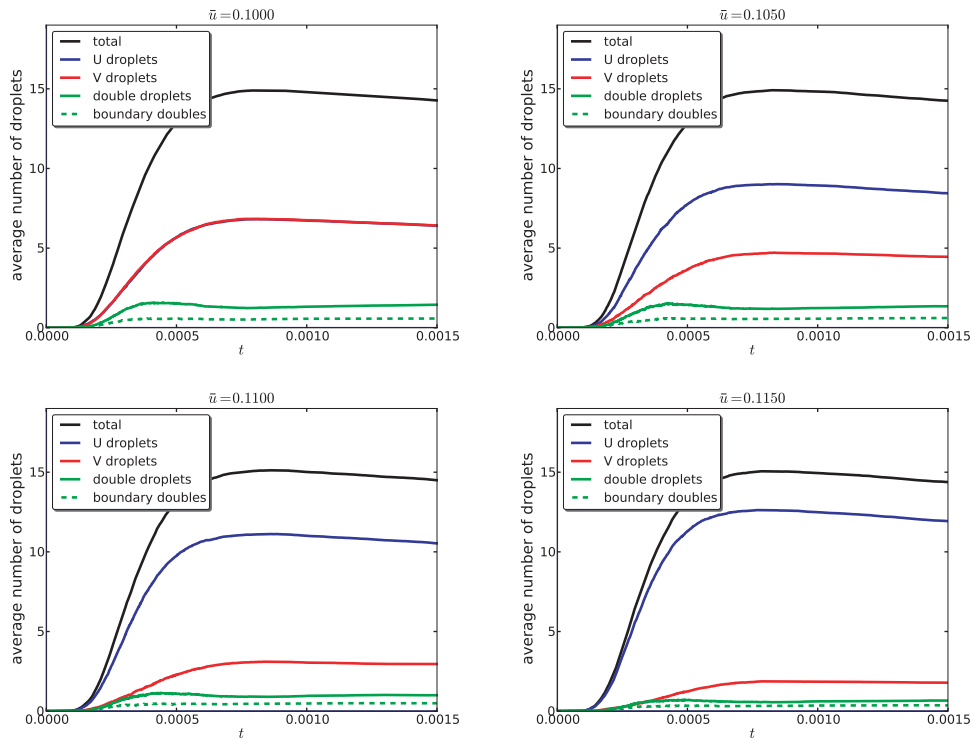


Figure 8. Averaged number of droplets as a function of time, organized by droplet composition. The graphs show the averaged total number of droplets (black), as well as the average number of u -droplets (blue), v -droplets (red), double droplets (solid green), and double droplets which touch the boundary (dashed green). From top left to lower right the images correspond to $\beta = k/200$ for $k = 0, 1, 2, 3$ with fixed $\alpha = 1/10$ in (18). The images show that while in the first case the average numbers of u - and v -droplets coincide, even a small increase in \bar{u} causes significant asymmetry between the u - and v -droplets. Double droplets are observed throughout all four images, but their frequency seems to decrease for increasing \bar{u} .

values close to 0.1. In fact, both the single and double droplet solutions are essentially stable in the region in which \bar{u} is close to 0.1, and the heteroclinic orbits for solutions emerging from the homogeneous initial state include connections to the double droplets.

3.3. Interaction length and domain scaling. At first glance, the evolution curves in Figure 8 seem to indicate a fundamental flaw in our simulations. As the time t ranges over the considered interval, the average total number of droplets reaches only about 15—with certain individual droplet counts in the single digits. How is it possible to draw any meaningful conclusions from this data, since the size and number of the droplets implies that the boundary of the domain is “nearby”? In other words, all of our observations could be due to boundary effects, and therefore they potentially have no bearing whatsoever on the bulk effects which can be observed far from the boundary. It is the aim of the current section to demonstrate that, surprisingly, the opposite is true. More precisely, we show that, in fact, it is possible to predict the average number of interior or boundary droplets for small values of the interaction length ε very accurately from information for relatively large values, such as the interaction length $\varepsilon = 0.05$ which was used in the previous section.

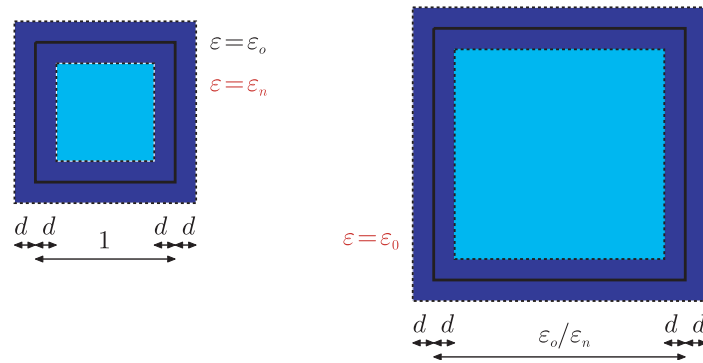


Figure 9. Domain scalings used for boundary and interior droplets. The left image shows the original domain $\Omega = (0, 1)^2$ at the interaction length ε_o . Performing a simulation on the same domain Ω , but with interaction length ε_n , amounts to considering $\varepsilon = \varepsilon_o$ on the new domain $\tilde{\Omega} = (0, \varepsilon_o/\varepsilon_n)^2$, as shown in the image on the right. The light and dark blue regions are used to predict the scaling behavior of the interior and boundary droplets, respectively.

To this end, consider again the Cahn–Morral system (12) on the domain $\Omega = (0, 1)^2$, say for an interaction length ε_o and noise strength σ_{noise} . One can easily see that decreasing the value of ε_o by a factor of $1/\gamma$, with $\gamma > 1$, is equivalent to keeping both the interaction length ε_o and the noise intensity σ_{noise} unchanged, but rescaling the domain by a factor of γ and the time by a factor of γ^2 . For this one just has to consider the new variables $\tilde{x} = \gamma x$ and $\tilde{t} = \gamma^2 t$ and keep the noise coefficients α_k in (13) fixed—but consider standard Brownian motions with respect to the new time \tilde{t} as well as rescaled basis functions φ_k , which form an orthonormal set on the larger domain $(0, \gamma)^2$. In other words, we keep the eigenvalues of the covariance operator Q associated with the noise process ξ fixed, and therefore also its trace. This rescaling is illustrated in Figure 9 for $\gamma = \varepsilon_n/\varepsilon_o$, where the left image shows the original domain $\Omega = (0, 1)^2$, and the right image the new domain $\tilde{\Omega} = (0, \varepsilon_n/\varepsilon_o)^2$. Since we are keeping the noise fixed, we can now assume that on average the droplet size is affected only by the interaction length ε . Thus simulations of (12) with $\varepsilon = \varepsilon_o$ on either Ω or $\tilde{\Omega}$ should produce droplets of comparable size. But how many droplets should we expect?

To begin with, consider droplets which nucleate along the boundary of the domain. If such droplets appear randomly, their number should scale with the length of the boundary. In other words, if for $\varepsilon = \varepsilon_o$ and the domain Ω the average number of droplets is given by b_o , then on the domain $\tilde{\Omega}$ one should expect $b_o \varepsilon_o/\varepsilon_n$ droplets. According to our above discussion, this would imply that if we consider (12) on the original domain Ω , but with interaction length $\varepsilon = \varepsilon_n$, then on average one should expect to see $b_o \varepsilon_o/\varepsilon_n$ droplets. In order to test this heuristic, we considered the symmetric mass case $\alpha = 1/10$ and $\beta = 0$ and performed 1024 Monte Carlo simulations each for a variety of ε -values. For each ε -value, we recorded the time at which the average total droplet count reached its maximal value, and compared the average number of boundary droplets at this time. The results of these computations are shown in the column labeled “Actual average” in Table 1, with the corresponding ε -values in column one. Now consider $\varepsilon_o = 0.05$, which represents the largest considered interaction length, i.e., the smallest number of boundary droplets. Using the scaling formula

$$b_n = b_o \cdot \frac{\varepsilon_o}{\varepsilon_n},$$

Table 1*Predicted and actual boundary droplet averages.*

Boundary droplet averages			
ε	Actual average	Predicted average	Relative error
0.050	7.37	7.37	0.00%
0.040	9.14	9.21	0.78%
0.030	12.17	12.28	0.87%
0.020	18.35	18.42	0.39%
0.010	36.75	36.84	0.24%
0.005	73.07	73.68	0.84%

Table 2*Predicted and actual interior droplet averages.*

Interior droplet averages			
ε	Actual average	Predicted average	Relative error
0.050	7.54	7.54	0.00%
0.040	12.66	12.66	0.00%
0.030	24.01	24.11	0.41%
0.020	58.04	58.01	0.05%
0.010	246.53	247.59	0.43%
0.005	1016.16	1022.18	0.59%

one can then predict the average number b_n of boundary droplets for any interaction length ε_n from the known average b_o . These predictions are listed in the third column of Table 1, with the corresponding relative prediction errors in column four—and they indicate that despite the small number b_o , accurate predictions for b_n can be made.

We now turn our attention to the case of interior droplets. From the same simulations as above, we also computed the average number of interior droplets for various ε -values, and the resulting counts are shown in the column labeled “Actual average” in Table 2. Again we are interested in whether it is possible to predict the average number i_n of interior droplets for some interaction length ε_n , from knowledge of the average interior droplet count i_o for a given $\varepsilon_o > \varepsilon_n$. For the interior droplets, one would expect a scaling proportional to the area of the domain, which would furnish $i_n = i_o \varepsilon_o^2 / \varepsilon_n^2$. However, further consideration makes it clear that this heuristic is incomplete, since it does not account for the part of the domain already occupied by boundary droplets.

As it turns out, the correct interpretation of the scaling behavior for interior droplets has to include a discussion of the boundary. Assuming again that the characteristic droplet thickness depends on the interaction length ε rather than the domain size of the two domains $\Omega = (0, 1)^2$ and $\tilde{\Omega} = (0, \varepsilon_o / \varepsilon_n)^2$, one would expect that there exists a boundary layer of fixed width d which does not play any role with respect to interior droplets. For this, see Figure 9, where light blue indicates the region responsible for the interior droplets, and dark blue the region responsible for the boundary droplets. (Note that this “extended area,” to account for “full” droplets via reflection, scales linearly with the perimeter.) Based on this, one would expect that i_n is given by the formula

$$i_n = i_o \cdot \frac{(\varepsilon_o / \varepsilon_n - 2d)^2}{(1 - 2d)^2},$$

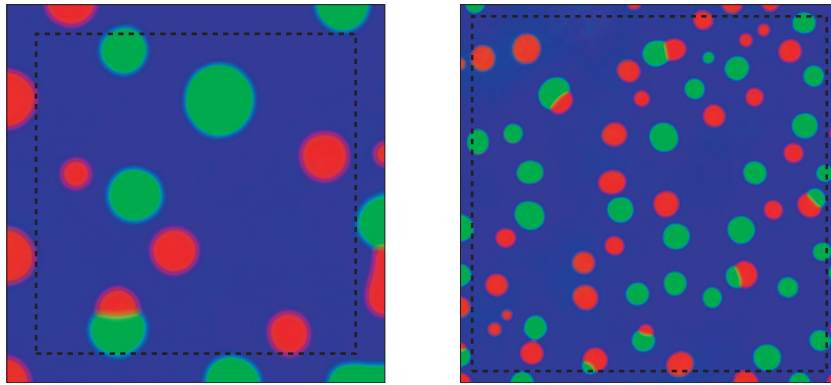


Figure 10. Sample alloy decompositions for $\varepsilon = 0.05$ (left) and $\varepsilon = 0.02$ (right). In both images, the border between the interior and the boundary regions is indicated by the dashed black line, based on the numerically determined value $d \approx 0.0772$.

where d denotes the characteristic width of the boundary layer, which can be determined by taking the average interior droplet counts from two distinct interaction lengths. The results of such a computation are shown in Table 2. In this case, we computed d from the two largest ε -values, which resulted in $d \approx 0.0772$. We then set $\varepsilon_o = 0.05$, and used the corresponding interior droplet count to predict i_n for the remaining smaller ε -values. The resulting predictions, including relative errors, are shown in the third and fourth columns of Table 2. These computations show that even interior droplet counts which are two orders of magnitude larger than i_o can be predicted accurately—even though for $\varepsilon_o = 0.05$ there are only a handful of interior droplets. Furthermore, in Figure 10 we indicate the border between the interior and the boundary region of the domain $\Omega = (0, 1)^2$ by a dashed black line for $\varepsilon = 0.05$ (left panel) and $\varepsilon = 0.02$ (right panel), based on the above value for d . These images indicate that the constant d is in fact a good measure for the typical size of a boundary droplet. We conclude this section by noting that in the context of a homological study of spinodal decomposition in the Cahn–Hilliard model [25], related scaling arguments have been used—yet without the identification of a boundary layer.

We would like to close this section with a brief discussion of the suitability of the Neumann boundary conditions which were used in our study. At first glance, the results of this section seem to indicate that their use, which is based on physically reasonable no-flux conditions, causes severe problems due to the resulting boundary effects. It is natural to wonder whether these issues could be avoided by imposing periodic boundary conditions, but this is not possible. The effects of a small domain do not disappear if one uses periodic boundary conditions. Assume, for example, that one uses boundary conditions of the form $u(x + L, y) = u(x, y + L) = u(x, y)$ for some periodicity $L > 0$. For fixed L , and if ε is too large, one can show that the size of the fundamental domain is too small to support droplet equilibria. In other words, once one fixes a periodicity L , one still has to choose ε sufficiently small in order to obtain a realistic model. Thus even in the periodic case, if ε is too large, one can see “boundary effects,” which in this case are due to the imposed length scale L .

4. Equilibrium solutions and nucleation pathways. In this section, we compute the set of low-energy equilibrium droplets within the nucleation region and numerically describe the

heteroclinic connections between these equilibria. As discussed in the introduction, the equilibria and their connecting orbits form the backbone of the global deterministic attractor of solutions expected when performing simulations in the stochastic setting. Our statistical data from the previous section raises a number of questions in terms of pattern selection, and we are able to answer several of these questions by considering the structure computed in this section.

4.1. Numerical methodology. We consider equilibria on a square domain which is small enough to support a single nucleating droplet. Due to the scaling relationship between domain size and interaction length, a small domain size is equivalent to considering a λ -value significantly smaller than those used in our previous simulations. For this section, we use $\lambda = 20$, which corresponds to $\varepsilon \approx 0.2236$. According to the discussion of the previous section, this choice results in an expected value of 0.05 interior droplets and 1.65 boundary droplets; i.e., with large probability one can expect roughly two boundary droplets (which are in fact half droplets) and no interior droplet. Assuming that the two half boundary droplets occur on opposite edges of the square, one can use symmetry arguments to combine the two boundary droplets into exactly one interior droplet. It turns out that this heuristic does indeed provide a reasonable choice of λ .

Finally, although the total mass distribution is conserved in both the deterministic and the stochastic evolution equation, the local mass on our small fundamental domains varies somewhat. This implies that understanding simulations for large domains with fixed values of α and β in fact involves considering equilibria on small domains for a range of local mass distributions. For the purposes of this section we again consider total mass vectors of the form

$$(\bar{u}, \bar{v}, \bar{w}) = (\alpha + \beta, \alpha - \beta, 1 - 2\alpha) \quad \text{with } \alpha = 0.1, |\beta| \leq 0.05.$$

This set is shown as a yellow line in Figure 3 and corresponds exactly to the initial conditions which were chosen for the Monte Carlo simulations of the previous section.

In order to compute the equilibrium solutions of the deterministic Cahn–Morrall system, we have to solve the elliptic system

$$(19) \quad \begin{aligned} -\Delta(\Delta u + \lambda f^{(u)}(u, v, w)) &= 0 & \text{in } \Omega, \\ -\Delta(\Delta v + \lambda f^{(v)}(u, v, w)) &= 0 & \text{in } \Omega, \\ -\Delta(\Delta w + \lambda f^{(w)}(u, v, w)) &= 0 & \text{in } \Omega, \end{aligned}$$

subject to homogeneous Neumann boundary conditions and the mass constraints

$$(20) \quad \begin{aligned} \frac{1}{|\Omega|} \cdot \int_{\Omega} u(x) \, dx &= \bar{u} = \alpha + \beta, \\ \frac{1}{|\Omega|} \cdot \int_{\Omega} v(x) \, dx &= \bar{v} = \alpha - \beta, \\ \frac{1}{|\Omega|} \cdot \int_{\Omega} w(x) \, dx &= \bar{w} = 1 - 2\alpha. \end{aligned}$$

In (19) we set $f(u, v, w) = (f^{(u)}(u, v, w), f^{(v)}(u, v, w), f^{(w)}(u, v, w))^t$ and use $\lambda = 1/\varepsilon^2$ as defined in (17). Our numerical computations are performed using the numerical continuation

package AUTO [19]. For this, we approximate the nonlinear left-hand side of (19) using a Galerkin spectral method which is based on the eigenfunctions of the Laplacian subject to homogeneous Neumann boundary conditions. This implementation is analogous to the one used in [17, 28], and we refer the reader to those papers for more details. For all of our simulations, we use approximations to the unknown functions with $30^2 = 900$ modes, which, due to the imposed mass constraints, amounts to 899 unknowns for the functions u and v , while the remaining function w is determined from $u + v + w = 1$. In addition to this general form of our numerical method, it turns out to be essential to address several issues that arise from the path-following method implemented in AUTO. These issues and their resolutions can be described as follows:

- Since AUTO uses the determinant of the Jacobian matrix to detect bifurcation points, it can in principle detect only bifurcation points with an odd-dimensional kernel. Unfortunately, in the situation of the Cahn–Morrall system on the square domain $\Omega = (0, 1)^2$, the symmetry of the domain frequently causes bifurcation points with two-dimensional kernels. In order to address this fact, we consider the elliptic system (19), (20) on the slightly perturbed domain

$$\Omega = (0, a_1) \times (0, a_2) \quad \text{with } a_1 = 1, a_2 = 0.95.$$

This asymmetry in the domain causes the splitting of the bifurcation points with two-dimensional kernels which are of interest to us into simple bifurcation points.

- The usage of the determinant of the Jacobian matrix in AUTO is also responsible for the second numerical issue that has to be addressed. Since we are working with high-dimensional algebraic systems which approximate an elliptic system, the fact that the eigenvalues of an elliptic operator quickly become unbounded as a function of the wave number leads to extremely large values of this determinant. In fact, as the continuation parameter increases, it quickly grows beyond the size of real numbers that can be represented in computer arithmetic. Thus, we employ an equation-by-equation scaling approach to control the size of the determinant, while at the same time not changing the solution set of the nonlinear system.

In addition to these two AUTO-specific issues, we also make use of the following dimension reduction in the case of equal minor masses:

- For some of our computations we will consider mass vectors $(\bar{u}, \bar{v}, \bar{w})$ with $\bar{u} = \bar{v}$; i.e., we consider the case $\beta = 0$. In this situation the solutions of interest will exhibit a reflection symmetry of the form

$$(21) \quad v(x, y) = u(1 - x, y) \quad \text{for all } 0 < x < a_1 = 1, 0 < y < a_2 = 0.95.$$

This symmetry allows us to reduce the elliptic system (19), (20) to a system for the unknown function u alone, and then recover v from (21) and w from the constraint $u + v + w = 1$.

More details about when this symmetry constraint is used will be described in the following section.

We would like to close this section with a second brief discussion comparing Neumann and periodic boundary conditions in the context of the numerical continuation methods discussed

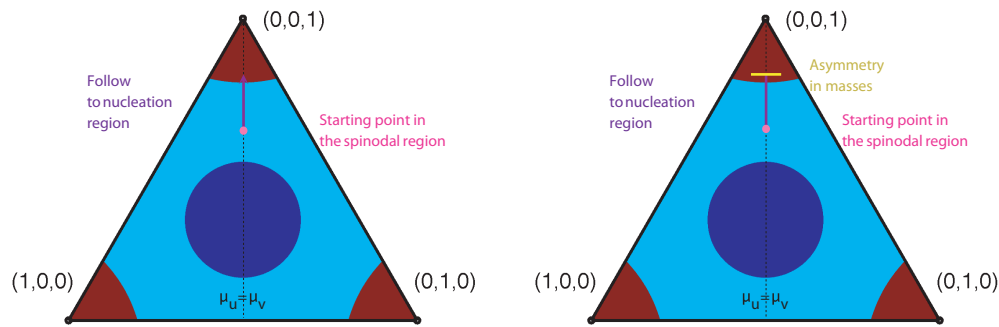


Figure 11. In order to find the equilibrium droplets in the metastable region we need to consider (19), (20) as a three-parameter continuation problem in λ , α , and β . We find the initial droplets in the spinodal region via continuation in λ , while the initial mass vector is kept fixed at the pink dot in the left panel. Then we continue these droplets into the metastable region through continuation in α (vertical arrow in the left panel), before finally using continuation with respect to β to find the droplets along the yellow line within the metastable region (right panel).

in this section. As with Neumann boundary conditions, periodic boundary conditions with the same period in horizontal and vertical directions result in symmetries which cause bifurcation points with kernels of dimension greater than one. In fact, while in the case of Neumann boundary conditions the problematic kernels have dimension two, under periodic boundary conditions they would have dimension four. Just as in the Neumann case, one could choose periodic boundary conditions with slightly unequal periods in the horizontal and the vertical directions, which would lead to the splitting of the bifurcation point into two with lower-dimensional kernels—but the kernel of each of these two bifurcation points would still be two-dimensional and therefore pose a computational problem. In the periodic case, the additional high dimensionality of the kernel is due to the fact that periodic boundary conditions also introduce translational invariances, which are not present with Neumann boundary conditions. In order to overcome the resulting computational issues it would be necessary to introduce a phase condition, resulting in extra computational cost.

4.2. Interior droplets in the spinodal region. As mentioned earlier, our goal is to find droplet equilibrium solutions of the system (19) subject to the mass constraint (20) for mass vectors $(\bar{u}, \bar{v}, \bar{w})$ in the metastable region. As such, it seems natural to initialize the continuation method with the known homogeneous equilibrium $(\bar{u}, \bar{v}, \bar{w})$ and use parameter continuation with respect to increasing λ to find nontrivial solution branches. Yet, as we have seen in section 2.2, within the metastable region this homogeneous state is stable for all $\lambda > 0$. In other words, there will be no solution branches which bifurcate from the homogeneous state in the metastable region.

In order to avoid the above problem we proceed as follows. Consider the initial mass vector corresponding to $\alpha = 0.125$ and $\beta = 0$; i.e., consider the vector

$$(\bar{u}, \bar{v}, \bar{w}) = (0.125, 0.125, 0.75),$$

which lies in the spinodal region. This starting point is indicated by a dot in the two images of Figure 11. Keeping this mass vector fixed, we can now try to find nontrivial solution branches

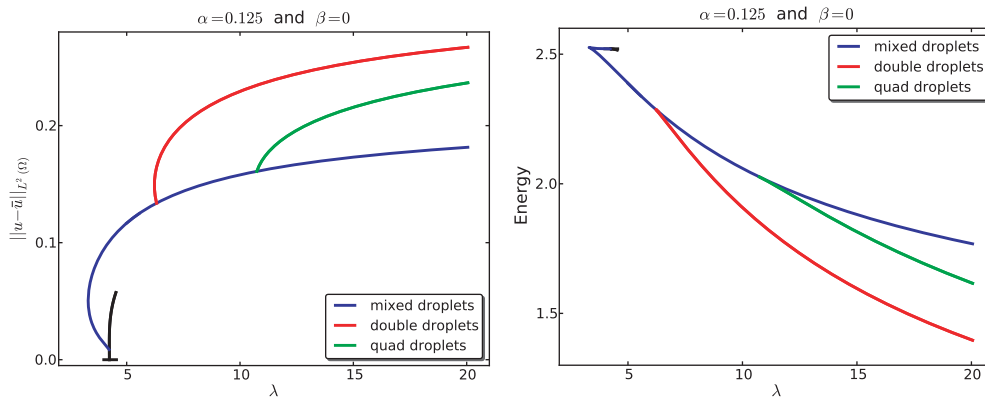


Figure 12. Partial bifurcation diagram for (19), (20) for $\alpha = 0.125$ and $\beta = 0$. In the left diagram, the small horizontal black line segment is part of the trivial homogeneous solution branch. From this branch, a primary nontrivial branch bifurcates in the direction of the eigenfunction in (22), which is shown vertically in black. This latter branch undergoes a symmetry breaking bifurcation leading to the blue secondary branch which, together with the red and green ternary branches, contains isolated droplet solutions. The right diagram shows the solution energies of the same branches as functions of λ .

which bifurcate from the homogeneous equilibrium as λ increases. As in our discussion in section 2.2, one can easily find the potential bifurcation points, which according to our use of the perturbed domain are all simple bifurcation points.

For our applications we are interested in only solutions whose geometry is of droplet structure. Since the geometry of the solutions on a bifurcating branch is initially determined by the kernel functions at the bifurcation points, one can easily see that the single droplet solutions have to be created within the first few bifurcating branches. Our numerics shown in Figure 12 demonstrate that the droplet equilibria lie on certain secondary bifurcation branches which bifurcate from one specific primary branch, as well as on certain ensuing ternary branches. The primary branch in turn bifurcates from the homogeneous trivial solution branch in the direction of the kernel function

$$(22) \quad c \cdot \begin{pmatrix} 1 \\ 1 \\ -2 \end{pmatrix} \cdot \cos \frac{2\pi y}{a_2}.$$

Thus, close to the bifurcation branch the level curves $u = \bar{u}$ of the solution component u are close to parallel horizontal lines. A short distance from the bifurcation point on the trivial solution branch the primary branch undergoes a secondary bifurcation. This bifurcation breaks the symmetry of the level curve $u = \bar{u}$ and leads ultimately to the merging of the two horizontal level curves to form a single closed curve—resulting in an isolated droplet. Two ternary branches which emanate from the secondary branch contain the remaining interior droplet solutions.

The basic bifurcation structure described above is shown in the left diagram of Figure 12. The small horizontal black line segment is part of the trivial homogeneous solution branch, and part of the bifurcating primary branch is shown vertically in black. The symmetry breaking bifurcation leads to the secondary branch, which is shown in blue. This secondary branch

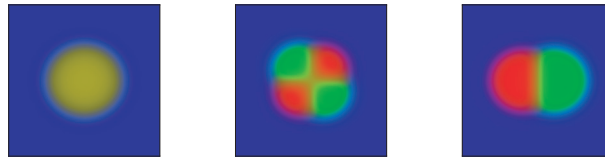


Figure 13. Isolated droplet solutions for system (19) subject to the mass constraint (20) for $\alpha = 0.125$, $\beta = 0$, and $\lambda = 20$. The three solutions correspond to the three endpoints of the blue, green, and red branches in Figure 12; i.e., they are ordered with respect to decreasing energy.

contains a number of bifurcation points, only two of which are of interest to us and are indicated in Figure 12. The emanating red and green branches lead to isolated droplets, while the remaining bifurcations from the blue branch furnish solutions which are not of this form. While the right diagram in Figure 12 shows the same branches, but now in a diagram of λ versus energy, the geometry of the solutions on these branches is shown in Figure 13. Note that even though the branches of Figure 12 are shown as curve segments, they actually are doubly covered smooth curves. In the case of the blue branch, the droplet shown in Figure 13, which consists of a homogeneous mixture of the two minor components and will be called a *mixed droplet* from now on, occurs on only one of the two halves of the branch, while the other half contains two half droplets which are located at the left and right vertical edges of the domain. This latter solution is, of course, uninteresting for our purposes. On the other hand, the two halves of the green branch do contain two interior droplets, which will be called *quad droplets* from now on—the one shown in the middle of Figure 13, as well as the one which is obtained by exchanging green and red. Analogously, the two halves of the red branch contain two different *double droplets*. Finally, one obtains similar droplets if one considers the primary branch which bifurcates from the homogeneous trivial solution in the direction of the eigenfunction $(1, 1, -2)^t \cdot \cos(2\pi x)$. Since these can essentially be obtained from the droplets above via rescaling in the coordinate axes and rotating by ninety degrees, it suffices to only consider the droplets above.

4.3. From the spinodal to the metastable region. Having identified the three main types of interior droplets, one can now proceed to continue these nontrivial solutions into the metastable region. This is accomplished as outlined in Figure 11(left). By now keeping $\beta = 0$ and $\lambda = 20$ fixed, each of these solutions can be continued with respect to α . This is indicated by the vertical blue arrow in Figure 11. The results of this continuation are shown in Figure 14. In all three cases, the solutions form a simple closed curve in function space, which extends well into the metastable region. Since we are interested specifically in the case $\alpha = 0.1$, we determine all solutions on these branches at this parameter value. The following criteria allow us to limit our consideration to a small number of droplet solutions:

- The mixed droplet branch has exactly four solutions at $\alpha = 0.1$, which are shown in Figure 15. Only two of these solutions, namely the first and the third, are interior droplets. We will not consider the remaining ones further. Notice that both the first and the third solutions consist of a droplet which contains an equal and homogeneous mixture of the two minor components. Yet, the first solution has an extremely small amplitude. We refer to these first and third solutions, respectively, as the small and mixed solutions.

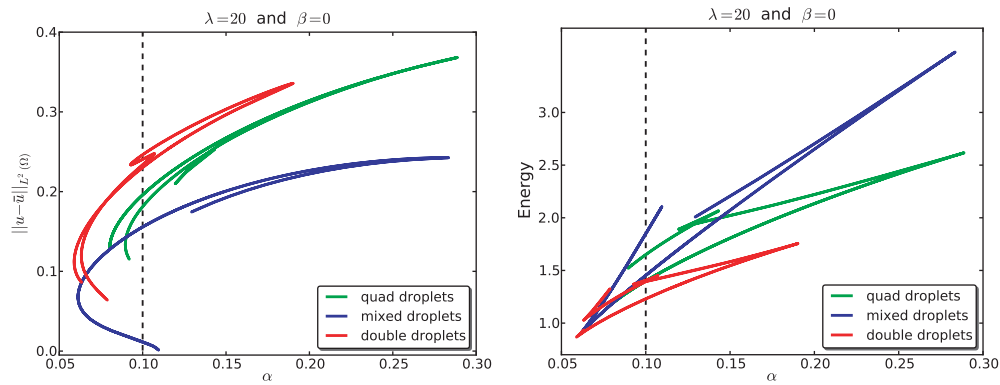


Figure 14. Solution branches as functions of α , for fixed $\lambda = 20$ and $\beta = 0$, which originate at the three solutions shown in Figure 13. In each case, the branch consists of a simply closed curve, so the curves shown in the figure are all doubly covered.



Figure 15. Solutions of the mixed droplet branch in Figure 14 with $\alpha = 0.1$. There are four equilibria, which are ordered by decreasing energy. A careful examination shows that the first two solutions shown are both nonhomogeneous, with a droplet respectively in the middle and on the sides. Due to symmetry, the first two solutions have the same energy, as do the last two.

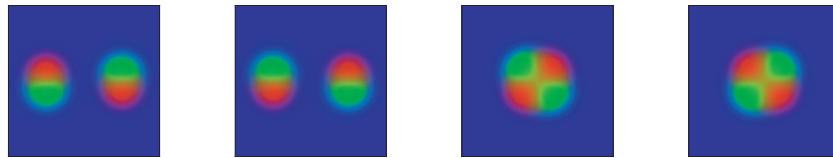


Figure 16. Solutions of the quad droplet branch in Figure 14 with $\alpha = 0.1$. There are four equilibria, which are ordered by decreasing energy. Due to symmetry, the first two solutions have the same energy, as do the last two.

- Similarly, the quad solution branch has exactly four solutions at $\alpha = 0.1$, which are shown in Figure 16. Note that the first two would be equivalent if we were considering periodic boundary conditions. However, only the last two of these solutions are single interior droplets. We will therefore not consider the remaining ones further. By symmetry, we need to perform numerics on only one of these two remaining double solutions, as the details of the other one follow directly from the symmetry of exchanging u and v .
- Finally, the double solution branch gives rise to exactly eight solutions at $\alpha = 0.1$, which are shown in Figure 17. Again only the last two of these are single interior droplets, and only these will be considered further. As in the quad case, we need to

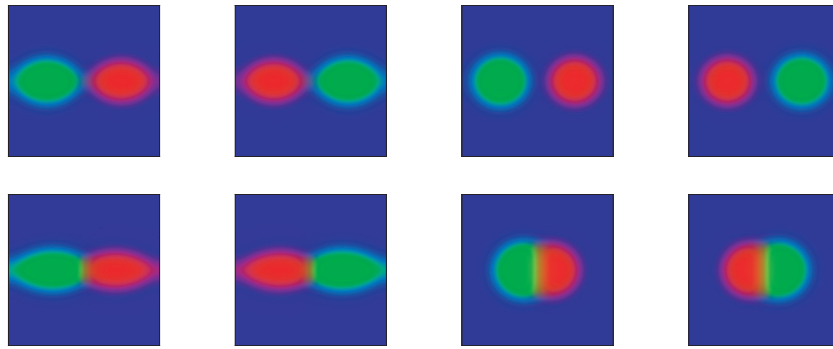


Figure 17. Solutions of the mixed droplet branch in Figure 14 with $\alpha = 0.1$. There are eight equilibria, which are ordered by decreasing energy from top left to bottom right. Due to symmetry, equilibria which can be transformed into each other by exchanging green and red have the same energy.

consider numerically only one of the two solutions, as they are related by an exchange of u and v .

We have thus reduced consideration to four nonhomogeneous droplet solutions. Note that all the computations of this section and of section 4.2 used the symmetry reduction mentioned at the end of section 4.1. Thus, we used AUTO on the reduced 899-dimensional system which uses (21).

4.4. Droplet branches during metastability. As a final step we now use the four initial interior droplets for $\lambda = 20$ and $\alpha = 0.1$ which were identified in the last section, and perform continuation with respect to the parameter β . In doing so, we cover the yellow line segment which is shown in Figure 11(right). For this continuation, one has to consider the full system (19) subject to the mass constraint (20), i.e., without the symmetry condition (21). This is due to the fact that only in the equal minor mass case $\beta = 0$ can one expect the symmetry condition to be satisfied. Thus, the numerical computations in this section use AUTO on a 1798-dimensional algebraic system, which determines the 899 modes for the unknown functions u and v .

The bifurcation diagram resulting from the above computations is shown in Figure 18, with two close-ups contained in Figure 19. The β -values in these diagrams basically parametrize the yellow line in Figure 11. It turns out that for each of the four interior droplets identified in the last section—the low- and high-amplitude mixed droplets, the quad droplet, and the double droplet—continuation with respect to β furnishes a simply closed curve. These curves are shown in Figure 18 in yellow, blue, green, and red, respectively. In addition, these bifurcation diagrams show the trivial homogeneous equilibrium, which is always stable, as a dashed black curve. Since all of the nontrivial bifurcation branches are in fact simply closed curves, all of these curves in the bifurcation diagrams are in fact doubly covered, so each point on these curves gives two solutions. In some cases, for example in the case of the mixed droplets, the additional droplets are in fact two half droplets located at opposite edges of the base domain—and are therefore uninteresting for our application. Yet in other cases, the additional droplets correspond to exchanging the location of the minor phases. This will be described in more detail below.

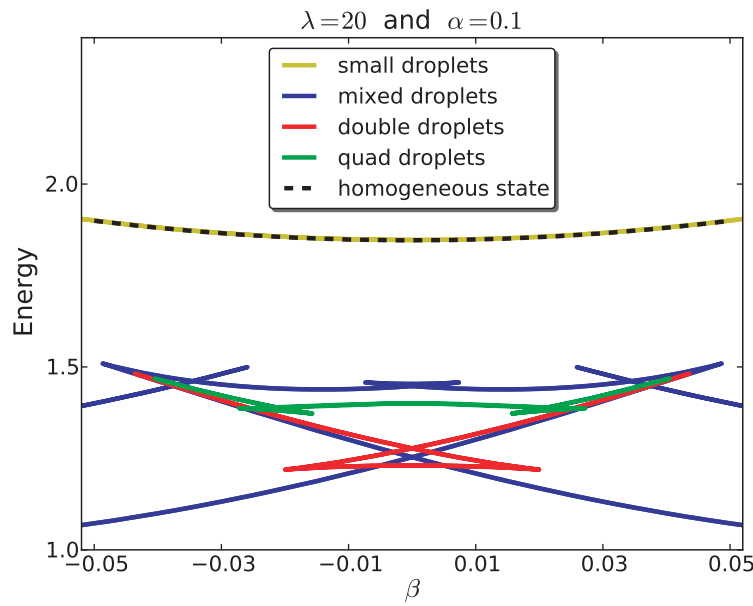


Figure 18. Bifurcation diagram for interior droplets in the metastable region. The β -values in the diagram basically parametrize the yellow line in Figure 11. The green and red curves are obtained via continuation from the quad- and double droplets in Figures 16 and 17. The blue and yellow curves are obtained via continuation from the high- and low-amplitude mixed droplets in Figure 15. The dashed black curve shows the trivial homogeneous equilibrium.

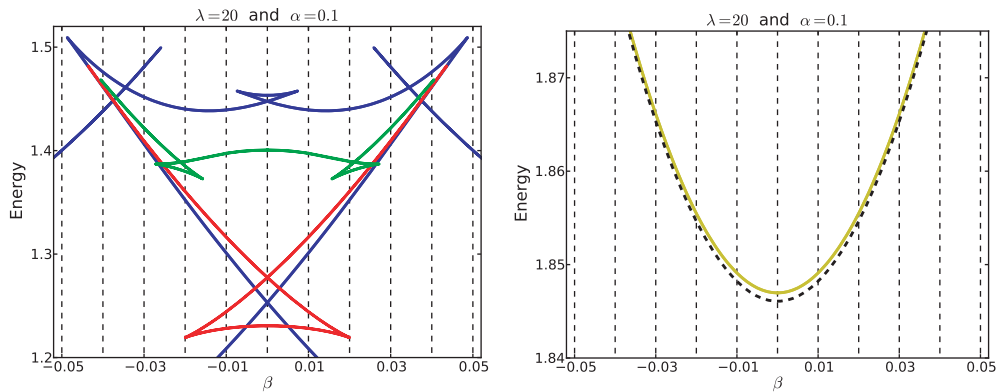


Figure 19. Close-ups of the bifurcation diagram in Figure 18. The left diagram shows the three lower energy branches, while the right diagram shows the two high-energy ones.

Before taking a closer look at the geometry of the interior droplets for the equal minor mass case, a few interesting observations can be made already from the bifurcation diagram in Figure 18.

- Close to—in the sense of energy difference—the trivial homogeneous steady state $(\bar{u}, \bar{v}, \bar{w})$ there is a nontrivial droplet solution with slightly higher energy. Specifically, we have seen in the last section that this solution is the low-amplitude “small” mixed solution found in section 4.3. Thus, one can expect that this solution takes on

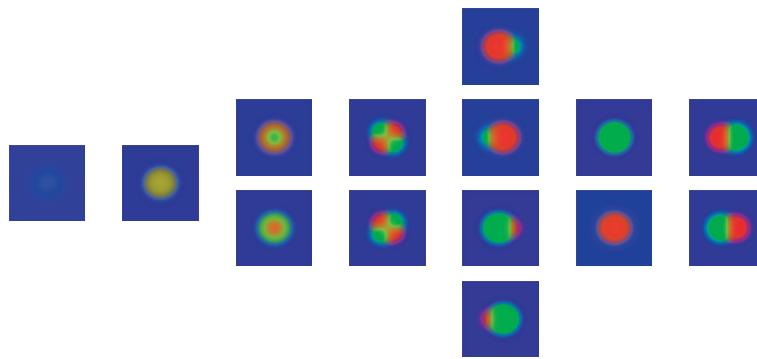


Figure 20. Droplet geometries for the case $\lambda = 20$, $\alpha = 0.1$, and $\beta = 0$, i.e., for the equal minor mass case $\bar{u} = \bar{v} = 0.1$, $\bar{w} = 0.8$. The droplets are ordered from left to right according to decreasing energy. Droplets in the same column have the same energy.

the role of the canonical nucleus in [2]. Note that this canonical nucleus does not yet select any of the two minor phases, but rather considers a homogeneous mixture of them.

- The lower part of the double droplet branch in the left diagram of Figure 19 exists only for β -values between -0.02 and 0.02 , which corresponds to $0.08 \leq \bar{u} \leq 0.12$. Notice that this is exactly the range in the droplet likelihoods shown in Figure 7 during which double droplets can be observed.



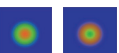




To shed further light on the information provided by the bifurcation diagram in Figure 18, we mainly concentrate on the equal minor mass case $\beta = 0$ for the remainder of this paper. In this situation, the geometry of the resulting interior droplets is shown in Figure 20. These droplets are ordered from left to right with respect to decreasing energy; droplets in the same column have the same energy. Comparing these droplets to actual numerically computed solution paths, such as the one shown in Figure 4, one can recognize almost all of these during the evolution—except for the quad droplets. Furthermore, assuming that the above-mentioned role of the small-amplitude mixed droplet is that of a canonical nucleus saddle solution which directs the dynamics to the large-amplitude mixed droplet, it seems plausible that the material selection within a droplet happens only after the initial phase separation, and that this selection is coordinated in fact by the large-amplitude mixed droplet, which therefore serves as an organizing center for the droplet dynamics. This will be investigated further in the next section.

We close this section with a comment on the completeness of the bifurcation diagram shown in Figure 18. Apart from obvious extensions due to symmetry arguments, we do expect this bifurcation diagram to contain most of the interior droplet solutions of the Cahn–Morral system in the considered mass range. In fact, for the remainder of this paper we concentrate on the interesting case of β being close to zero, and for these β -values we expect the diagram to contain all possible interior droplets. While this statement cannot be justified rigorously in our numerical setting, we will see in the next section that further droplet solutions are unlikely to exist.

4.5. Morse decompositions and nucleation pathways. This final section is devoted to the actual droplet dynamics in the most interesting equal minor mass case $\beta = 0$. For this,

Table 3

Interior droplet equilibria for $\beta = 0$ together with their indices. The droplets are ordered from top to bottom with respect to their energy. The total index is shown in the last column. The second and third columns further divide the unstable eigenvalues into strongly and weakly positive eigenvalues. See the text for further information.


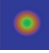



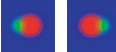
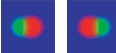

	Type	Strongly positive	Weakly positive	Index
	Mixed	1	2	3
	Mixed	2, 1, 2, 1	2	8
	Mixed	2, 2, 1	2	7
	Quad	1, 2	3	6
	Double	1	3	4
	Mixed	0	2	2
	Double	0	3	3

we restrict our attention to the deterministic Cahn–Morral system and try to numerically determine a Morse decomposition of interior droplets, as well as a description of the heteroclinic orbits connecting them. As we have mentioned earlier, our main philosophy is that nucleation on a large domain happens through several nucleation events on smaller fundamental domains, on which it is driven by general large deviations types results. This intuition was based on the recent work [41], which considers nucleation for the stochastic Allen–Cahn equation and for which the fundamental domains could be treated as independent. In our situation, the global mass conservation of the Cahn–Morral system will cause our fundamental domains to not be independent. In fact, we do expect that the effective total mass in each fundamental domain will be different from—albeit close to—the overall mass constraint. As a result, even for the study of the equal minor mass case $\beta = 0$ one has to consider the bifurcation diagram for all values of $\beta \approx 0$. Thus, we will in the following concentrate on the interval $-0.015 \leq \beta \leq 0.015$.

As a first step towards the above goal one has to determine the stability of the droplet equilibria. For this we again employ a spectral method approach; i.e., we apply a Galerkin spectral method to approximate the right-hand side of the linearized Cahn–Morral system (11) at a given droplet. The eigenvalues of the resulting matrix, which acts on the 1798 modes describing the approximations of the u and v components, are then determined using standard eigenvalue computation methods. The results of this eigenvalue computation for the interior droplets at the parameter values $\lambda = 20$, $\alpha = 0.1$, and $\beta = 0$, i.e., for the equal minor mass case, are shown in Table 3. Analogous results for the right endpoint $\beta = 0.15$ of our considered β -interval are contained in Table 4. In each of these two tables, the first column shows the interior droplets, ordered from top to bottom with respect to their energy, and the second column denotes the branch on which the droplet can be found in Figure 18. The total index of each droplet is listed in the last column. Of more interest to us is a further partition of the positive

Table 4

Interior droplet equilibria for $\beta = 0.15$ together with their indices. The droplets are ordered from top to bottom with respect to their energy. The total index is shown in the last column. The second and third columns further divide the unstable eigenvalues into strongly and weakly positive eigenvalues, as before.

	Type	Strongly positive	Weakly positive	Index
	Mixed	1	2	3
	Mixed	2, 2, 1	2	7
	Quad	2, 1	3	6
	Double	1	3	4
	Mixed	0	2	2
	Double	1	3	4
	Double	0	3	3
	Mixed	0	2	2

eigenvalues of a droplet, which is listed in the third and fourth columns of the table. The third column shows the number of eigenvalues which are significantly positive, grouped according to multiplicity, while the fourth column lists the number of weakly positive eigenvalues, i.e., eigenvalues which are positive but close to zero. For example, the large-amplitude mixed droplet has six strongly unstable directions, which is indicated by the sequence 2, 1, 2, 1. This sequence also encodes the fact that the largest and the third-largest eigenvalues each have multiplicity two, while the second- and fourth-largest eigenvalues are simple. In addition, the large-amplitude mixed droplet has two weakly positive eigenvalues.

While the strongly positive eigenvalues of the interior droplets depend on the specific droplet under consideration, the weakly positive eigenvalues can easily be explained as follows. Since we are looking for equilibrium solutions of (19), (20) which are of droplet structure, these solutions will be almost constant along the boundary of the domain Ω . This implies that if the even extension of such a solution is translated or rotated slightly, it will still “almost” satisfy the nonlinear elliptic system on the domain Ω . While in general this perturbed function is not an exact solution, this fact will introduce, however, two (in the case of almost radially symmetric solutions) or three (in the case of radially asymmetric solutions) eigenvalues of the linearization of (19) at this equilibrium which are close to zero. This heuristic can easily be verified in Tables 3 and 4. All droplets have either two or three small positive eigenvalues, and the ones with three eigenvalues are exactly the ones which are not almost radially symmetric. Note that these small eigenvalues have to be positive, since for the Cahn–Morrall system one would expect the global energy minimizers to form droplets along the boundary of the domain—ore precisely, in the corners. In other words, the interior droplets all have to be unstable, and the small positive eigenvalues allow the dynamics to translate and rotate the solution into the right position.

In order to numerically determine the possible connections between the interior droplets, we proceed as follows. For each of the droplets, we compute not only the eigenvalues of the linearization (11), but also the corresponding eigenfunctions. We then use a spectral time-stepping code similar to the one in [28] to compute solution paths of the full deterministic Cahn–Morrall system (12) originating at the functions

$$(u_0, v_0, w_0) \pm \delta \cdot \psi,$$

where (u_0, v_0, w_0) denotes the droplet solution of (19), (20), the function $\psi : \Omega \rightarrow \mathbb{R}^3$ denotes an eigenfunction of the linearization, and $\delta > 0$ is small. In other words, the function ψ satisfies the system

$$\begin{aligned} -\Delta (\varepsilon^2 \Delta \psi - PD_u^2 F(u_0, v_0, w_0) \psi) &= \kappa_\psi \psi && \text{in } \Omega, \\ \frac{\partial \psi}{\partial \nu} &= \frac{\partial \Delta \psi}{\partial \nu} = 0 && \text{on } \partial \Omega, \\ \psi_1 + \psi_2 + \psi_3 &= 0, \end{aligned}$$

where κ_ψ denotes the associated eigenvalue; see also (11). The resulting solution paths were followed until the solution seemed to converge to one of the droplets.

The resulting numerical Morse decomposition for the equal minor mass case, i.e., for the parameter values $\lambda = 20$, $\alpha = 0.1$, and $\beta = 0$, is shown in the left diagram of Figure 21; the one for $\beta = 0.015$ is shown on the right. In these diagrams, we omit interior droplets which can be obtained from another one by exchanging red and green, except if this omission would confuse the overall picture. The arrows indicate numerically verified connections, and the colors of the arrows correspond to the instability of the respective eigendirections. In other words, black arrows correspond to runs with ψ being an eigenfunction for the largest positive eigenvalue, blue arrows correspond to the second-strongest eigenvalue, etc. We would like to note that in general it is extremely difficult to numerically verify heteroclinic connections between saddle equilibria using the above simplistic approach. However, we are interested mostly in the possible transitions from high-index droplets to those with no strongly unstable directions—and these can be verified. This is due to the fact that the motion of the droplets caused by the small positive eigenvalues is extremely slow, and therefore from a numerical point of view our solution paths do seem to converge. Thus we do not claim that the connections indicated in Figure 21 are “minimal,” i.e., that they consist of exactly one true heteroclinic. It is certainly possible that an arrow in the diagram in reality corresponds to a sequence of heteroclinics. In some cases, however, our numerics did indicate connections between high-index droplets, and in these cases we include this information in the diagram.

In terms of describing the dynamics of interior droplets in the equal minor mass case, the left diagram of Figure 21 provides some interesting insight.

- As we mentioned before, the small-amplitude mixed droplet has a strongly unstable manifold of dimension one, one branch of which converges to the stable homogeneous state. The second branch, however, converges directly to the large-amplitude mixed solution.
- The large-amplitude mixed droplet acts as the main distribution point for the droplet dynamics. Its two largest eigenvalues direct solutions to the effectively stable double

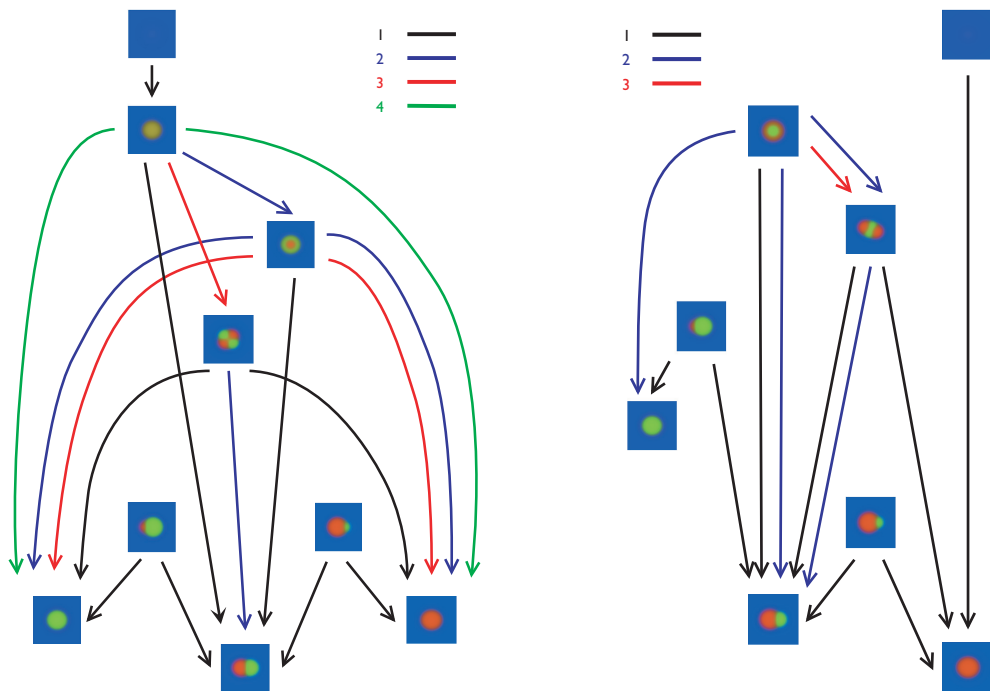


Figure 21. Numerically computed Morse decompositions for the interior droplets of Table 3 (left panel) and of Table 4 (right panel), *i.e.*, for the case $\lambda = 20$, $\alpha = 0.1$, and $\beta = 0$ (left) or $\beta = 0.015$ (right). These heteroclinic connections have been computed numerically in the directions of the eigenfunctions of the linearized system (11) at the droplets, and the colors correspond to the level of instability of the eigenfunctions. In other words, black arrows correspond to the strongest unstable direction, blue arrows to the second-strongest, etc.

droplet, as well as to the at first glance unphysical ring droplet. These ring droplets, however, are frequently observed in numerical simulations. On the other hand, the quad solutions can be reached only in the directions of the third largest eigenvalues and are therefore very unlikely to be observed in actual simulations.

- The pure droplets appear to be reachable only from the large-amplitude mixed droplet via the fourth-largest eigenvalues, which seems very unlikely in general. However, both the second- and the third-largest eigenvalues of the ring droplet direct droplets towards these pure states.
- The asymmetric double droplets are saddle solutions at the boundary of the domain of attraction of the pure and the symmetric double droplets. As such, they can only be observed as transitional states.

At first glance, these observations seem to indicate that the most likely droplets in the equal minor mass case should be the double droplets—a guess which is quickly disproved by a glance at the solution path of Figure 4. In order to address this discrepancy, we recall that in some (maybe even many) fundamental domains the effective total mass will satisfy $\beta \neq 0$. We therefore also have to understand the Morse decompositions for these cases, and in order to keep the scope of this paper reasonable we consider only the case $\beta = 0.015$, which is shown in Figure 21(right). From this diagram we can make the following observations:

- In the case $\beta = 0.015$ the large-amplitude mixed solution no longer exists, and our numerics show that the canonical nucleus directs droplets to the pure droplet of the larger minor phase.
- While the Morse decomposition still indicates the existence of paths towards the pure droplet of the smaller minor phase or the double droplet, these can no longer be reached from the one-dimensional unstable manifold of the small-amplitude mixed droplet which sits at the boundary of the domain of attraction of the homogeneous state.

In other words, in the asymmetric case $\beta \neq 0$, we expect droplets to be directed to the pure droplet of higher mass with higher probability. Since one of our main points was that on a large domain one can discuss nucleation by means of smaller fundamental domains, the effective total mass on these smaller domains does in fact select which specific Morse decomposition is responsible for the droplet dynamics. It is not surprising that, due to the global mass conservation in the Cahn–Morral system, these fundamental domains are in fact correlated—which leads to mass fluctuations between these fundamental domains. Thus, even if on the large domain Ω one considers the case $\beta = 0$, there will be smaller fundamental domains which effectively have $\beta \neq 0$. This fact explains both the high probability of occurrence of the pure droplets, as well as the observation of effectively stable double droplets for values of β somewhat outside of the interval $[-0.02, 0.02]$; see again Figures 7 and 18.

5. Conclusions and future directions. In this paper, we have studied nucleation in three-component alloys as modeled by the stochastic Cahn–Morral system (12). We approached this problem from two distinct perspectives:

- On the one hand, we have performed Monte Carlo–type simulations of the stochastic evolution equation, for varying mass of the initial homogeneous state in the metastable region. These simulations furnished detailed information on the likelihood of occurrence of certain droplets. It also enabled us with the help of scaling methods to quantitatively determine the characteristic size of the droplet or, in other words, the width of the region experiencing boundary effects.
- In addition, we have used numerical continuation techniques to determine equilibrium states of the deterministic Cahn–Morral system, which are in the form of interior droplets. We have found that these droplets, as well as the parameter ranges over which they can be found, are in good agreement with the results from the Monte Carlo simulations.

While the above results provide a first insight into the nucleation dynamics of ternary alloys, there are several further avenues of research to be addressed in the future. On the one hand, it would be valuable to validate the equilibrium droplets and the associated Morse decompositions via rigorous computational techniques. Furthermore, we have concentrated our discussion on the bifurcation diagram and the associated Morse decompositions close to the symmetric case $\beta = 0$, but it would be very useful to further determine and validate the bifurcation diagram for larger values of $|\beta| > 0$. Finally, it would be interesting to investigate the effect of the noise intensity and of the spatial correlation of the noise on the characteristic size of the droplets and the size of the boundary layer. These topics, however, are beyond the scope of the current paper and will be addressed elsewhere.

Acknowledgments. T. W. would like to acknowledge the hospitality of the Isaac Newton Institute in Cambridge, UK, where part of this research was performed.

REFERENCES

- [1] R. A. ADAMS, *Sobolev Spaces*, Academic Press, San Diego, London, 1978.
- [2] P. W. BATES AND P. C. FIFE, *The dynamics of nucleation for the Cahn–Hilliard equation*, SIAM J. Appl. Math., 53 (1993), pp. 990–1008.
- [3] D. BLÖMKER, B. GAWRON, AND T. WANNER, *Nucleation in the one-dimensional stochastic Cahn–Hilliard model*, Discrete Contin. Dynam. Systems, 27 (2010), pp. 25–52.
- [4] D. BLÖMKER, S. MAIER-PAAPE, AND T. WANNER, *Spinodal decomposition for the Cahn–Hilliard–Cook equation*, Comm. Math. Phys., 223 (2001), pp. 553–582.
- [5] D. BLÖMKER, S. MAIER-PAAPE, AND T. WANNER, *Surface roughness in molecular beam epitaxy*, Stoch. Dyn., 1 (2001), pp. 239–260.
- [6] D. BLÖMKER, S. MAIER-PAAPE, AND T. WANNER, *Phase separation in stochastic Cahn–Hilliard models*, in Mathematical Methods and Models in Phase Transitions, A. Miranville, ed., Nova Science Publishers, New York, 2005, pp. 1–41.
- [7] D. BLÖMKER, S. MAIER-PAAPE, AND T. WANNER, *Second phase spinodal decomposition for the Cahn–Hilliard–Cook equation*, Trans. Amer. Math. Soc., 360 (2008), pp. 449–489.
- [8] J. W. CAHN, *Free energy of a nonuniform system. II. Thermodynamic basis*, J. Chem. Phys., 30 (1959), pp. 1121–1124.
- [9] J. W. CAHN AND J. E. HILLIARD, *Free energy of a nonuniform system I. Interfacial free energy*, J. Chem. Phys., 28 (1958), pp. 258–267.
- [10] J. W. CAHN AND J. E. HILLIARD, *Free energy of a nonuniform system III. Nucleation in a two-component incompressible fluid*, J. Chem. Phys., 31 (1959), pp. 688–699.
- [11] C. CARDON-WEBER, *Cahn–Hilliard stochastic equation: Existence of the solution and of its density*, Bernoulli, 7 (2001), pp. 777–816.
- [12] CHOMP, *Computational Homology Project*, software available online at <http://chomp.rutgers.edu>, 2002–2010.
- [13] H. COOK, *Brownian motion in spinodal decomposition*, Acta Metallurgica, 18 (1970), pp. 297–306.
- [14] G. DA PRATO AND A. DEBUSSCHE, *Stochastic Cahn–Hilliard equation*, Nonlinear Anal., 26 (1996), pp. 241–263.
- [15] G. DA PRATO AND J. ZABCZYK, *Stochastic Equations in Infinite Dimensions*, Cambridge University Press, Cambridge, UK, 1992.
- [16] A. C. DAVISON AND D. V. HINKLEY, *Bootstrap Methods and Their Application*, Cambridge University Press, Cambridge, UK, 1997.
- [17] J. E. DEERING, *Computation of the Bifurcation Structure of the Cahn–Hilliard Equation*, Master’s thesis, Department of Applied Mathematics and Statistics, University of Maryland, Baltimore County, Baltimore, MD, 2002.
- [18] J. P. DESI, E. SANDER, AND T. WANNER, *Complex transient patterns on the disk*, Discrete Contin. Dynam. Systems, 15 (2006), pp. 1049–1078.
- [19] E. DOEDEL, *AUTO: A program for the automatic bifurcation analysis of autonomous systems*, in Proceedings of the Tenth Manitoba Conference on Numerical Mathematics and Computing, Vol. I (Winnipeg, MB, 1980), 30 (1981), pp. 265–284.
- [20] C. M. ELLIOTT AND S. LUCKHAUS, *A Generalized Diffusion Equation for Phase Separation of a Multi-component Mixture with Interfacial Free Energy*, Preprint 195, Sonderforschungsbereich 256, Bonn, 1991.
- [21] D. J. EYRE, *Systems of Cahn–Hilliard equations*, SIAM J. Appl. Math., 53 (1993), pp. 1686–1712.
- [22] D. J. EYRE, *Cascades of spinodal decompositions in the ternary Cahn–Hilliard equations*, in Mathematics of Microstructure Evolution, L. Q. Chen, B. Fultz, J. W. Cahn, J. R. Manning, J. E. Morral, and J. A. Simmons, eds., The Minerals, Metals & Materials Society, Warrendale, PA, 1996, pp. 367–378.
- [23] P. C. FIFE, *Models for phase separation and their mathematics*, Electron. J. Differential Equations, 2000 (2000), pp. 1–26.

- [24] M. I. FREIDLIN AND A. D. WENTZELL, *Random Perturbations of Dynamical Systems*, 2nd ed., Springer-Verlag, New York, 1998.
- [25] M. GAMEIRO, K. MISCHAIKOW, AND T. WANNER, *Evolution of pattern complexity in the Cahn-Hilliard theory of phase separation*, *Acta Materialia*, 53 (2005), pp. 693–704.
- [26] B. GAWRON, *Nucleation in the One-dimensional Cahn-Hilliard Model*, Ph.D. thesis, Institut für Mathematik, RWTH Aachen, Aachen, Germany, 2006.
- [27] C. P. GRANT, *Slow motion in one-dimensional Cahn–Morrall systems*, *SIAM J. Math. Anal.*, 26 (1995), pp. 21–34.
- [28] T. HARTLEY AND T. WANNER, *A semi-implicit spectral method for stochastic nonlocal phase-field models*, *Discrete Contin. Dynam. Systems*, 25 (2009), pp. 399–429.
- [29] P. C. HOHENBERG AND B. I. HALPERIN, *Theory of dynamic critical phenomena*, *Rev. Modern Phys.*, 49 (1977), pp. 435–479.
- [30] J. J. HOYT, *Spinodal decomposition in ternary alloys*, *Acta Metallurgica*, 37 (1989), pp. 2489–2497.
- [31] J. J. HOYT, *The continuum theory of nucleation in multicomponent systems*, *Acta Metallurgica et Materialia*, 38 (1990), pp. 1405–1412.
- [32] J. J. HOYT, *Linear spinodal decomposition in a regular ternary alloy*, *Acta Metallurgica et Materialia*, 38 (1990), pp. 227–231.
- [33] S. MAIER-PAAPE AND U. MILLER, *Path-following the equilibria of the Cahn-Hilliard equation on the square*, *Comput. Visualization Sci.*, 5 (2002), pp. 115–138.
- [34] S. MAIER-PAAPE, B. STOTH, AND T. WANNER, *Spinodal decomposition for multi-component Cahn-Hilliard systems*, *J. Statist. Phys.*, 98 (2000), pp. 871–896.
- [35] S. MAIER-PAAPE AND T. WANNER, *Spinodal decomposition for the Cahn-Hilliard equation in higher dimensions. Part I: Probability and wavelength estimate*, *Comm. Math. Phys.*, 195 (1998), pp. 435–464.
- [36] S. MAIER-PAAPE AND T. WANNER, *Spinodal decomposition for the Cahn-Hilliard equation in higher dimensions: Nonlinear dynamics*, *Arch. Ration. Mech. Anal.*, 151 (2000), pp. 187–219.
- [37] J. E. MORRAL AND J. W. CAHN, *Spinodal decomposition in ternary systems*, *Acta Metallurgica*, 19 (1971), pp. 1037–1045.
- [38] E. SANDER AND T. WANNER, *Monte Carlo simulations for spinodal decomposition*, *J. Statist. Phys.*, 95 (1999), pp. 925–948.
- [39] E. SANDER AND T. WANNER, *Unexpectedly linear behavior for the Cahn–Hilliard equation*, *SIAM J. Appl. Math.*, 60 (2000), pp. 2182–2202.
- [40] J. D. VAN DER WAALS, *The thermodynamic theory of capillarity flow under the hypothesis of a continuous variation in density*, *Verh. Konink. Akad. Wetensch. Amsterdam*, 1 (1893), pp. 1–56.
- [41] E. VANDEN-EIJNDEN AND M. G. WESTDICKENBERG, *Rare events in stochastic partial differential equations on large spatial domains*, *J. Statist. Phys.*, 131 (2008), pp. 1023–1038.
- [42] T. WANNER, *Maximum norms of random sums and transient pattern formation*, *Trans. Amer. Math. Soc.*, 356 (2004), pp. 2251–2279.